



Dense Point Cloud Quality Factor as Proxy for Accuracy Assessment of Image-Based 3D Reconstruction

Farid Javadnejad, Ph.D., M.ASCE¹; Richard K. Slocum²; Daniel T. Gillins, Ph.D., P.L.S., M.ASCE³; Michael J. Olsen, Ph.D., M.ASCE⁴; and Christopher E. Parrish, Ph.D.⁵

Abstract: Photogrammetry using structure from motion (SfM) and multiview stereopsis (MVS) techniques can recover three-dimensional (3D) structure from a set of overlapping, unoriented, and uncalibrated images captured by nonmetric digital cameras. It is possible to generate accurate reconstructions of sparse points using mathematically robust bundle adjustment procedures together with accurate surveying control data. However, MVS, which recovers the dense geometry by matching and expanding between sparse points, is prone to additional error. Miscellaneous constituents such as sensor specifications, data collection, and site conditions can introduce random noise or artifacts that locally degrade the accuracy of the dense point cloud. This paper proposes seven indexes, named dense point cloud quality factors (DPQFs), as proxy indicators of image-based dense reconstruction accuracy. DPQFs include proximity to keypoint features, distance to GCPs, angle of incidence, camera stand-off distances, number of overlapping images, brightness index, and darkness index. The correlation between the DPQFs and the 3D error was investigated in simulated and empirical experiments scenarios with varying factors. The results of this study showed that the DPQFs provide proxy indications for accuracy when the error estimation for the dense point clouds is more challenging than error propagation computations in bundle adjustment (BA). The DPQFs can be defined solely using the SfM-MVS data, without prior knowledge about the error. Inclusion of the factors as additional fields of information and their visualization provide tangible intuitions regarding the factors that influence the accuracy of image-based 3D reconstruction. DOI: [10.1061/\(ASCE\)SU.1943-5428.000333](https://doi.org/10.1061/(ASCE)SU.1943-5428.000333). © 2020 American Society of Civil Engineers.

Author keywords: Image-based reconstruction; Dense point cloud; Quality factor; Accuracy; Unmanned aircraft systems (UAS).

Introduction

High-resolution three dimensional (3D) data are essential for detailed spatial interpretation and analysis in many geomatics applications (Abellan et al. 2016; Che and Olsen 2017; Javadnejad et al. 2013, 2017b, 2019; Mahmoudabadi et al. 2016; McCaffrey et al. 2005; O'Banion et al. 2019; Olsen et al. 2015; Omasa et al. 2006; Sohn and Dowman 2007; Wood et al. 2017). Increasingly, modern photogrammetry utilizing consumer-grade nonmetric cameras, mostly mounted on small unmanned aircraft systems (UAS), is being used to generate the high-resolution 3D data. Because of the widespread availability, low maintenance cost, ease of operation,

low-altitude maneuvering capability, and flexible and frequent data collection, UAS-based photogrammetry is changing the surveying and mapping research and industry (Colomina and Molina 2014; Pajares 2015). UAS-based photogrammetry has been tested in different environments, and its advantages and disadvantages have been explored (Faraji et al. 2016; Gao et al. 2017; Griffin 2014; Javadnejad 2018; O'Banion et al. 2018; Shi et al. 2016; Wood et al. 2017). A number of open-source programs such as VisualSfM and Bundler (Snavely et al. 2006), as well as commercial packages such as PhotoScan Professional version 1.4, now named Metashape, and Pix4DMapper Pro version 4.0 commonly are used for processing the imagery collected from UAS platforms to generate high-resolution mapping products such as 3D point clouds, mesh surfaces, digital terrain models (DTMs), and orthoimages.

Photogrammetry from nonmetric digital cameras includes using structure from motion (SfM) and multiview stereopsis (MVS) techniques that recover structure from a set of overlapping unoriented and uncalibrated images and generate 3D dense point clouds (Eltnier et al. 2016; Furukawa and Ponce 2010; Seitz et al. 2006). The general steps for SfM photogrammetry are shown in Fig. 1. The processing starts with automatic extraction of key features from the raw imagery (Harris and Stephens 1988; Lowe 1999; Snavely et al. 2008; Szeliski 2010; Tomasi and Kanade 1992). Then the extracted features are described in multidimensional descriptors, e.g., scale invariant feature transform (SIFT) (Lowe 1999, 2004). The procedure is followed by matching the features (Snavely et al. 2008; Szeliski 2010) and outlier rejection (Crandall et al. 2013; Fischler and Bolles 1981). Subsequently, the bundle adjustment (BA) (Shum et al. 1999; Triggs et al. 1999) simultaneously solves for the intrinsic orientation (IO) and extrinsic orientation (EO) parameters of the cameras and generates a sparse point cloud by minimizing the reprojection error of feature matches in the form of a

¹Formerly, Graduate Research Assistant, School of Civil and Construction Engineering, Oregon State Univ., 101 Kearney Hall, Corvallis, OR 97331 (corresponding author). ORCID: <https://orcid.org/0000-0001-9942-8442>. Email: fijnje@lifetime.oregonstate.edu

²Graduate Research Assistant, School of Civil and Construction Engineering, Oregon State Univ., 101 Kearney Hall, Corvallis, OR 97331. Email: slocumr@oregonstate.edu

³Geodesist, National Geodetic Survey, National Oceanic and Atmospheric Administration, 1315 East-West Highway, Silver Spring, MD 20910. Email: daniel.gillins@noaa.gov

⁴Professor, School of Civil and Construction Engineering, Oregon State Univ., 101 Kearney Hall, Corvallis, OR 97331. Email: olsen@oregonstate.edu

⁵Associate Professor, School of Civil and Construction Engineering, Oregon State Univ., 101 Kearney Hall, Corvallis, OR 97331. Email: chris.parrish@oregonstate.edu

Note. This manuscript was submitted on June 23, 2019; approved on June 9, 2020; published online on September 23, 2020. Discussion period open until February 23, 2021; separate discussions must be submitted for individual papers. This paper is part of the *Journal of Surveying Engineering*, © ASCE, ISSN 0733-9453.

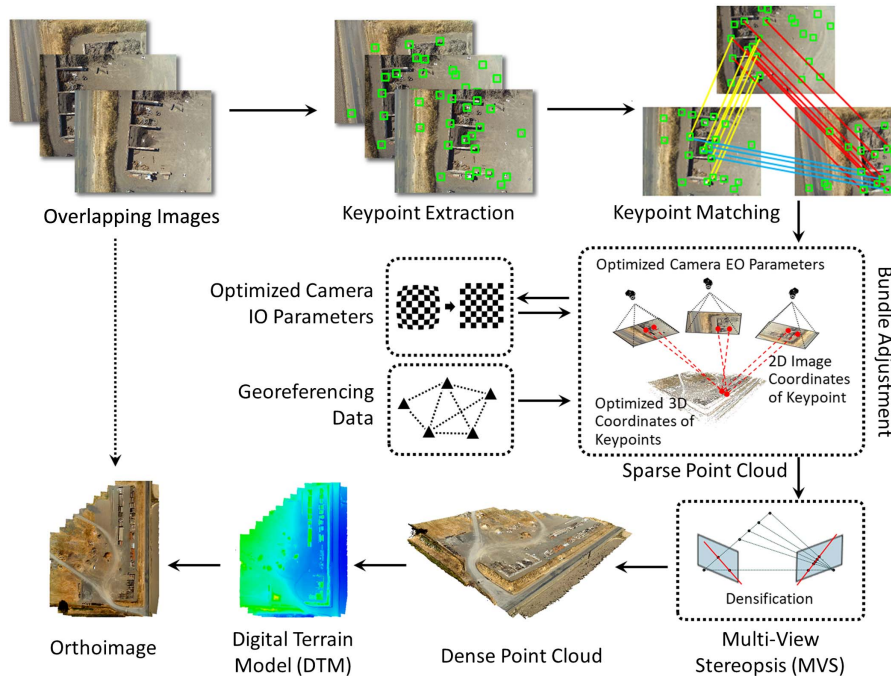


Fig. 1. Steps of SfM-MVS processing. (Reproduced with permission from Javadnejad 2018.)

sparse point cloud (Crandall et al. 2013; Snavely et al. 2008; Szeliski 2010). The reconstructed model is transformed to a real-world coordinate system using either known ground control point (GCP) coordinates or via UAS-based global navigation satellite system (GNSS) camera pose estimations (Javadnejad and Gillins 2016). In addition to georeferencing the SfM point clouds, the use of GCPs also can improve the accuracy of the model by a second step of the BA to reoptimize the solution after the initial relative BA based on feature matches. In this step, the camera parameters and the constructed geometry are reoptimized after importing the GCPs (Shum et al. 1999).

The sparse point cloud ordinarily is complemented with a densification step through MVS processing, which generates a depth map for pixels of the image based on photoconsistency in an oriented block obtained from bundle adjustment (Furukawa and Ponce 2010; Remondino et al. 2014; Snavely et al. 2008). Together with accurate input data, it is possible to produce an accurate reconstruction of sparse points using the mathematically robust BA procedure. On the other hand, MVS, which recovers the densified point cloud by matching and expanding between sparse points may yield results with different and inconsistent accuracies. MVS works by enforcing epipolar geometry constraints obtained from BA solution, and later filtering the outliers (Furukawa and Ponce 2010). MVS algorithms are being improved continuously in terms of accuracy and completeness. Identifying and recognizing the sources of reconstruction error, and estimating the accuracy and reliability of the MVS-SfM results are ongoing research topics (Furukawa and Ponce 2010; Yao et al. 2014; Zhu et al. 2015). Many research studies have investigated the applicability of the technique for a variety of mapping instances; in addition, more research is studying the accuracy of SfM-MVS products [e.g., Javadnejad (2018) and references therein].

Uncertainty in image-based 3D reconstruction is a function of various input data factors and processing parameters, such as the quality of the input image, accuracy, number and distribution of ground control points, the accuracy of IO and EO parameters, certainty in feature detection, matching in overlapping images, and

choice of reconstruction technique (Hofsetz et al. 2004; Seitz et al. 2006). The accuracy of SfM-MVS can be defined as the closeness of the empirical measurements to a reference ground truth, such as a comparison of SfM-MVS with a lidar point cloud or total station and/or GNSS measurements at checkpoints (CPs). Unlike GCPs, the CPs are not used for georeferencing or sparse point cloud optimizing; however, the known values of the CPs are compared with the coordinate measurements of the same points in the 3D geometry and are reported for accuracy assessment purposes (Javadnejad and Gillins 2016). In addition to empirical comparisons, Slocum and Parrish (2017) proposed a workflow which uses a simulated graphics environment for generating virtual UAS surveys to overcome challenges of empirical surveys such as the time and cost of data collecting campaigns. This approach incorporates the systematization of a reliable ground truth reference and leverages the isolation of environmental factors that contribute to error budget in SfM-MVS models, enabling investigation of the impact of individual parameters (Slocum and Parrish 2017).

In mapping and surveying applications, it has been found that the accuracy of SfM-MVS sparse and dense point clouds is influenced by many factors, such as image overlap, number of images, lens distortion model, number of ground control points, geometry of GCP distribution, geometry of camera distribution, accuracy of GCP or camera positions, image resolution, blurriness of imagery, noise of imagery, lighting condition, shadow effect, scene complexities, standoff distances, image-matching performance, image texture, presence of dense vegetation, moving objects in the scene, and user errors in selecting the image coordinates of GCPs (Agüera-Vega et al. 2017; Bolkas 2019; Carbonneau and Dietrich 2017; Clapuyt et al. 2016; Dandois et al. 2015; Eltner et al. 2016; Fonstad et al. 2013; González-Quiñones et al. 2018; Harwin et al. 2015; Harwin and Lucieer 2012; James et al. 2017a, b; Javadnejad et al. 2016, 2017a; Smith and Vericat 2015; Tonkin and Midgley 2016; Westoby et al. 2012).

This paper evaluated the utility of seven different factors, herein called dense point cloud quality factors (DPQFs), as proxy indicators for the accuracy of image-based reconstruction. Some of these

factors previously were identified as significant, as noted previously. This manuscript provides a mathematical definition for each factor and formulated their calculation from the input data used for SfM/MVS processing. The factors include (1) distribution of the keypoint features resulting from the BA, (2) distribution of GCPs, (3) angle of incidence, (4) camera stand-off distances, (5) number of images, (6) brightness index, and (7) darkness index. Although other studies presented the impact of some of these factors, this study investigated the correlation between these factors to outline the importance of each factor for different scenarios holistically. This research studied the correlation of the DPQF with reconstruction error for sets of simulated and empirical data with multiple scenarios. The work also is meant to help surveyors with planning the best data collection strategies for UAS/SfM photogrammetry projects to minimize error by defining indexes that can be optimized during data collection for improved accuracy. Furthermore, this paper supplemented the point cloud with additional quality indexes that can be helpful for visualization and identifying points that are prone to inaccurate reconstruction, and weighting for mesh generation. An advantage of the DPQFs is that the factors can be defined solely based on the inputs and results of SfM-MVS processing. They can provide a proxy indicator for dense point cloud quality, because the estimation of error for dense point clouds is more challenging than the error propagation estimation in BA.

Materials and Methods

This paper presents a simulated experiment based on the simUAS approach (Slocum and Parrish 2017) in which different scenarios for a scene were created, as well as an empirical case study exploring the use of both lidar and UAS for surveying a construction site. Digital photographs acquired from both data sets were postprocessed using SfM techniques to produce a high-resolution point cloud. The error is defined as the distance to the control data.

The ground truth for the simulated data is perfectly known and can be exported as a mesh model from the simulation environment, and the ground truth for the empirical data is the lidar. The resultant dense point clouds and error indexes were used to estimate the DPQF value, which subsequently was investigated for statistical correlation between all the factors and the error index to identify the impact and importance of each factor. Fig. 2 shows the approach used for estimating DPQF for both the simulated and empirical data sets.

Data Sets

Computer Graphics Simulation

The simulations were performed using Blender software version 2.78c, a free open-source 3D computer graphics software, following the simUAS approach (Slocum and Parrish 2017). The simulated scene was a site that consisted of a flat plane surface, 11 boxes, 7 horizontal cylinders representing pipes, 6 vertical cylinders, 3 spheres, 5 pyramids, 2 cones, and 3 icospheres of varying sizes (Fig. 3). The objects were textured using a variety of texture images acquired from freely available online data sets, such as brick, concrete, metal, wood, gravel, asphalt, and soil [Fig. 3(c)]. Two scenes, A and B, were generated by rendering two images to the ground planes. For Scene A, a 9,620 × 9,620-pixel image was generated by tiling six high-resolution aerial images with 10-cm pixel resolution [0.1 m ground sampling distance (GSD)] from Invercargill, New Zealand (LINZ 2016) [Fig. 3(a)]. The texture and objects in the images were sufficient for successful SfM-MVS pipeline feature extraction and matching. Moreover, the texture diversity in the image for the forest, residential, industrial, and water body areas allowed variation in DPQF values across the scene. For Scene B, a 50 × 50-pixel white Gaussian noise ($\sigma = 0.5$) was applied to the aerial image to manipulate the texture characteristics. Then it was overlaid with a transparent random noise image to ensure uniqueness in areas with blander texture, such as in the water and forest

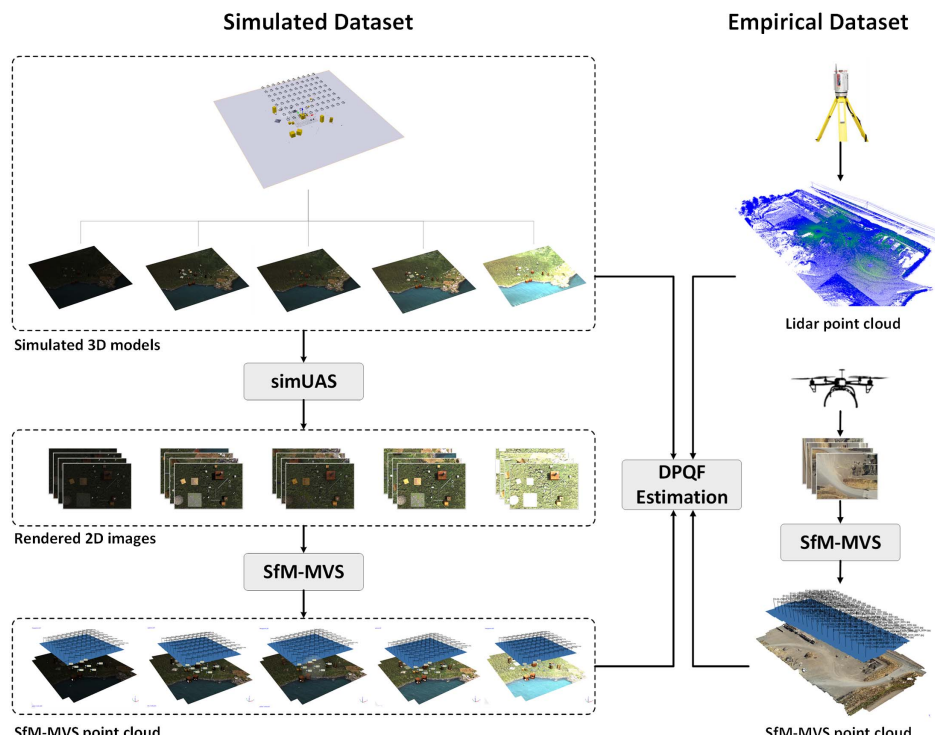


Fig. 2. Workflow for data preparation of simulated and empirical data sets, and DPQF estimation.

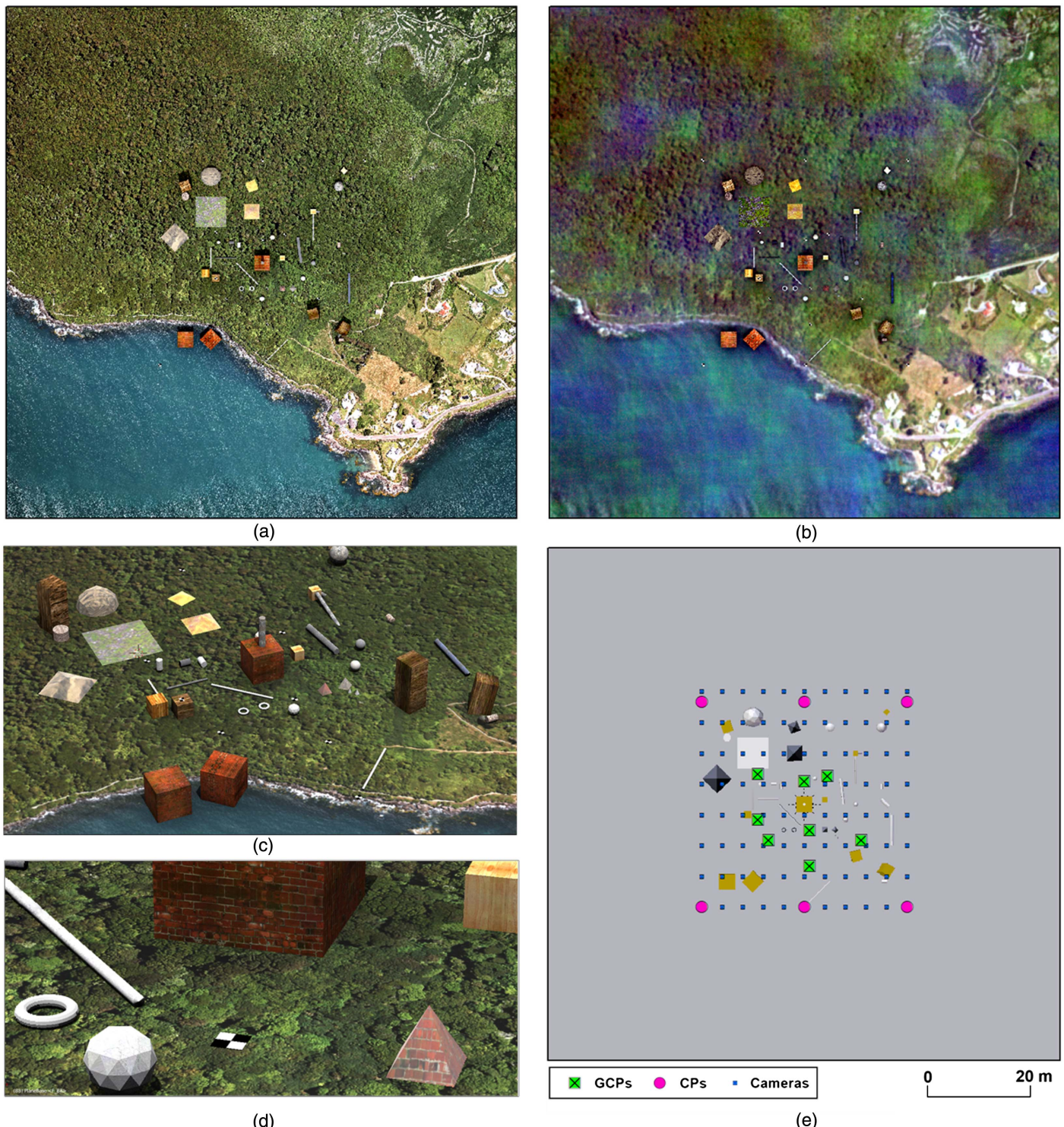


Fig. 3. (a) Overview of simulated Scene A; (b) overview of simulated Scene B; (c) different objects placed in the simulated scene with surface textures; (d) close-up view of textured objects and a black-and-white GCP on the scene; and (e) location of objects, GCPs, CPs, and the positions of cameras.

areas [Fig. 3(b)]. Scene B was a quick and easy way to add more variability to the texture resolved by the image, ensuring a broad range of textures. In both scenes, 14 black-and-white iron-cross targets similar to the one in Fig. 3(d) were placed in the scene. These targets were 1×1 m to resemble commonly used aerial targets in UAS photogrammetry.

Both scenes were illuminated with five different sun and ambient light intensities to create variation in lighting and shadows.

Fig. 4 shows the different lighting conditions in the simulation. Scenarios 1 and 5 were the darkest and brightest, allowing the existence of underexposed and overexposed object at the scene. Underexposure and overexposure occur when a camera sensor does not record enough details in the darkest and brightest parts of the images, respectively. Scenario 2 was brighter than the first scenario, with stronger sunlight and lower ambient light creating strong shadow areas. The higher ambient light intensity in Scenario 3

| Scenario | 1 | 2 | 3 | 4 | 5 |
|---------------|-----|-----|-----|-----|-----|
| Output | | | | | |
| Sun Light | 0.2 | 0.9 | 0.1 | 0.9 | 2.5 |
| Ambient Light | 0.2 | 0.1 | 0.9 | 0.9 | 2.0 |

Fig. 4. Sunlight and ambient light settings used for Scenarios 1–5 of A and B, and the resultant simulation for Scenarios A1–A5. The intensity values range between 0.0 and 10.0. With low values the sky has no sun, and with high values the sky has only sun.

minimized the intensity of shadow, and Scenario 4 had high sun and ambient light intensity creating appropriate contrast on textures (proper exposure). The impact of the different light on the accuracy of reconstruction is studied subsequently.

To simulate the UAS-based data collection, 88 cameras were positioned across the area including the simulated objects [Fig. 3(e)]. The camera was set to mimic a Sony A5000 (Sony City, Minato, Tokyo) with 16 mm focal length and output image sizes of $5,456 \times 3,632$ pixels. The simulated cameras were placed at 20-m above ground level (AGL) altitude and the flight lines were generated with respect to the height and width of the images to keep 80% of side and forward overlap. For Scenes A and B with the five different lighting scenarios, images were rendered at the given camera's locations using the Blender Internal Render Engine, and the resulting images were postprocessed using simUAS in MATLAB R2017a to add nonlinear Brown's lens distortion to the images. This approach was described in detail by Slocum and Parrish (2017). Overall, it took about 4 h to perform both the image rendering in Blender and the postprocessing in MATLAB for each experiment. In total, 10 experiments were simulated with Scenes A and B, with 5 different scenarios per scene using varying ambient lighting conditions (Fig. 4).

Empirical Case Study

The study area for the empirical assessment was a storage yard utilized by Linn County, Oregon, to store gravel, asphalt grindings, debris, spare concrete bridge parts, and piping material. It is located approximately 5 km northwest of the city of Lebanon (Fig. 5). The data for this site consisted of terrestrial lidar scan (TLS) data and the aerial imagery collected from a UAS. Prior to data collection, 18 aerial targets were established at the site on a grid pattern with 20

to 30 m spacing [Fig. 6(a)] that was used for georeferencing SfM-MVS data. The aerial targets, approximately 1 m^2 each, were nailed to the ground to ensure stability throughout the flight [Fig. 6(a)]. In addition, 38 color cross markings were placed on the existing pipes at the scene to check accuracy of the SfM results. Twelve boxes with four black-and-white targets on each face [Fig. 6(b)] were placed at intervals between the aerial targets. Only the black-and-white targets on the boxes were used for georeferencing the TLS data. Fig. 6(d) shows the layout of the control network. Repetitive 3-min observations were acquired on all aerial targets using a Leica GS14 (Heerbrugg, Canton St. Gallen, Switzerland) survey-grade GNSS receiver obtaining real-time kinematic corrections from the Oregon Real-Time GNSS Network (ORGN). The ORGN is a statewide real-time network managed by the Oregon Department of Transportation (ODOT 2020). In addition, all the aerial targets, markings, and box targets were surveyed using the radial traversing method with a Leica TS15 Total Station. It took 3.5 h to complete the ground surveying campaign to establish coordinates for the targets and the markings. The approach for a similar ground control network survey was described in more detail by Javadnejad and Gillins (2016).

The box targets [Fig. 6(b)] were placed strategically to be seen by the majority of the scans throughout the site by distributing the targets across the study area on a grid pattern with 15–20 m spacing [Fig. 6(d)]. The lidar data were collected via six separate scans using a Riegl VZ-400 (Horn, Lower Austria, Austria) scanner [Fig. 6(a)]. Each scan was 7 min in duration. In total, it took 1.5 h for the entire scan data collection, including setup and data capture times. A SenseFly Albris (Lausanne, Canton Vaud, Switzerland) (formerly known as the eXom) [Fig. 6(b)] was used to collect the aerial images. The flights were completed on August 17, 2016, under the Oregon State University (OSU) Certificate of Authorization (COA) for public UAS operations. The Albris had an integrated GNSS receiver and an inertial navigation system that allowed the craft to fly to predefined mission waypoints. The visible sensor on this platform was a Nokia camera (Espoo, Uusimaa, Finland) with a 10.01×7.51 -mm sensor and a 7.9-mm focal length, producing $7,152 \times 5,368$ -pixel images. The flights were performed such that nadir photographs were collected systematically with 80% side and 80% forward overlap at 45 m above the ground level, resulting in a ground sampling distance of 8 mm/pixel. The camera was triggered with automatic focus and exposure modes by the onboard autopilot system when the aircraft reached the preplanned flight mission waypoints [Fig. 6(c)]. In total, 95 images were collected during an 11-min flight.

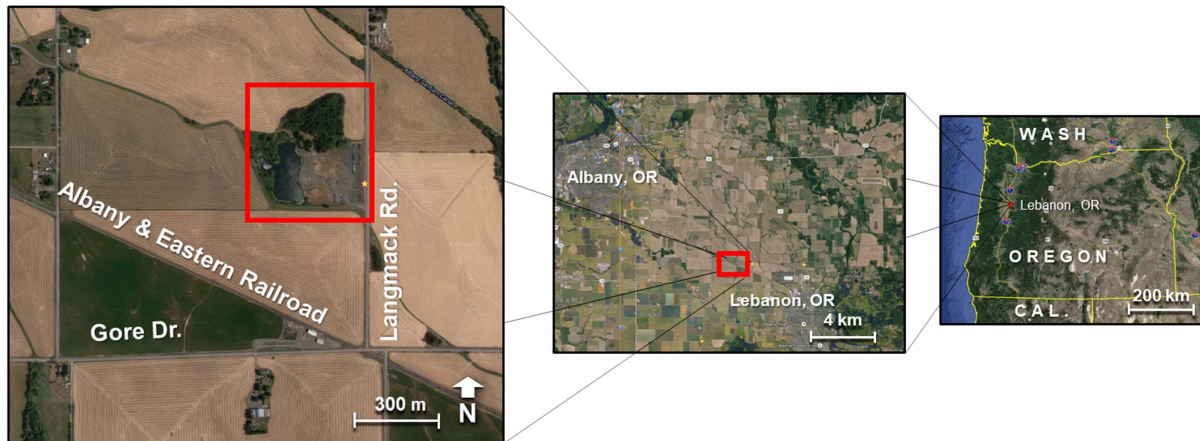


Fig. 5. Langmack storage facility. (Image data © 2017 Google Earth Landsat/Copernicus Data SIO, NOAA, U.S. Navy, NGA, GEBCO, and © 2017 Google Maps.)

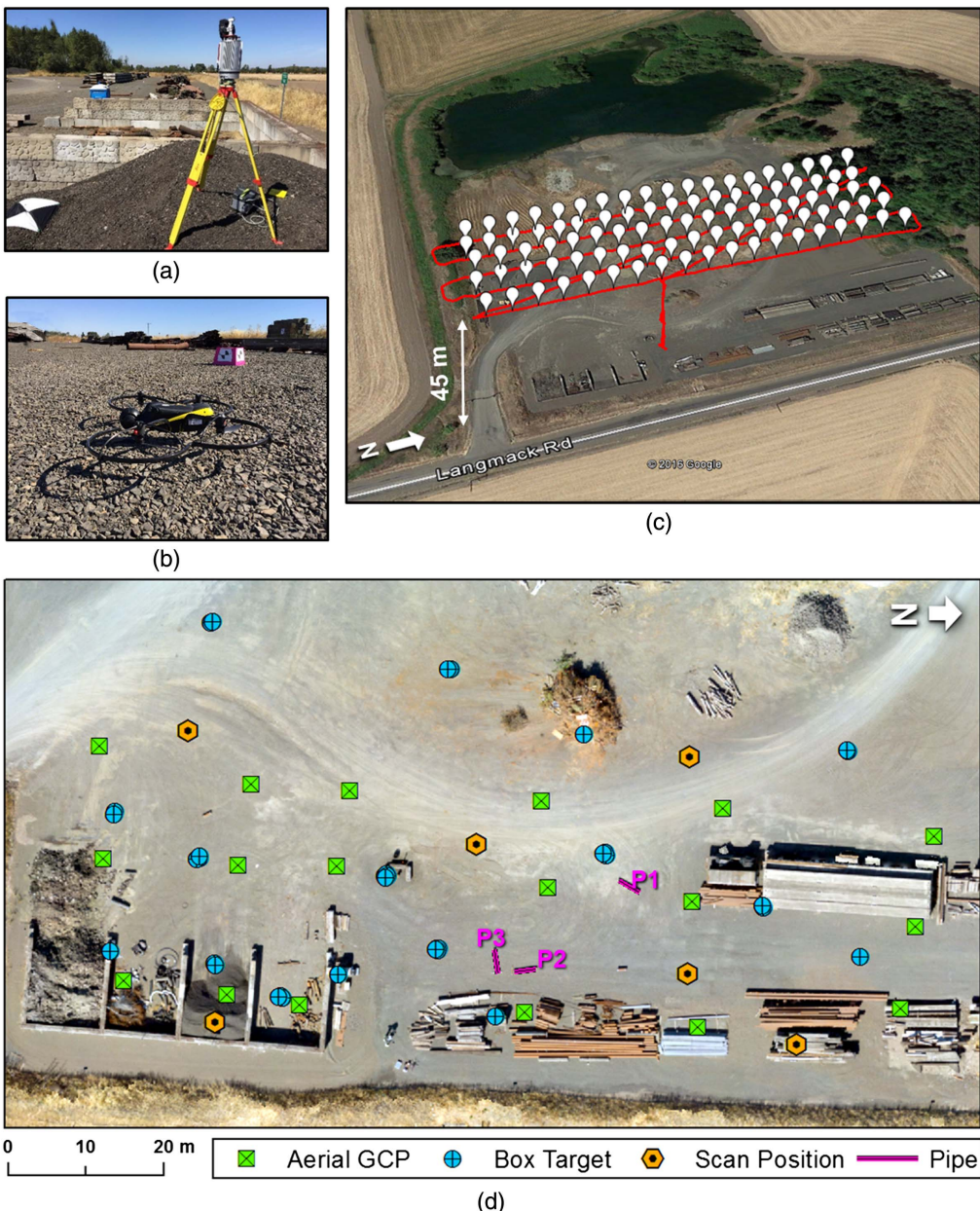


Fig. 6. (a) Riegl VZ400 and a nearby GCP; (b) Albris and a target box; (c) flight pattern; and (d) location of the established aerial targets, cross markings, box targets, and scan positions. [Images in Figs. 6(a and b) by the authors; image data in Fig. 6(c) Landsat/Copernicus © 2016 Google Earth.]

Point Cloud Generation

Simulated Data

The resulted imagery from simulations and the actual UAS operation at the Langmack site were processed using commercial software PhotoScan Pro 1.4. PhotoScan can generate point clouds, textured polygonal models, georeferenced orthoimages, and digital elevation model (DEM). In PhotoScan, the georeferencing is performed by identifying the GCPs in the photographs, inserting the coordinates and their standard deviation values, and/or by providing the location and orientation of the cameras. The exact position of the cameras, the camera calibration models, and 3D coordinates and pixel coordinates of the GCPs and CPs of the simulated scenes were imported to PhotoScan. The results for Simulation A3 are shown in Fig. 7, and the statistics of all SfM processing are listed in Table 1.

The final dense point clouds were processed using medium-quality and aggressive depth-filtering settings. The total processing time was 15 min for each scenario.

Empirical Data

For the Langmack data set, the control coordinates were determined by performing a least-squares adjustment (LSA) on the network of Total Station and GNSS observations with Star*NET version 8.0 using the approach described by Javadnejad and Gillins (2016). The adjustment resulted in an estimated horizontal and vertical RMS error (RMSE) of 1.97 and 2.8 mm, respectively, for the ground control network coordinates. The resultant coordinates were used to postprocess the 95 aerial images collected during the UAS flights in PhotoScan. The data were reprocessed for the 5 scenarios selecting 4, 6, 8, 12, and 18 GCPs from the aerial

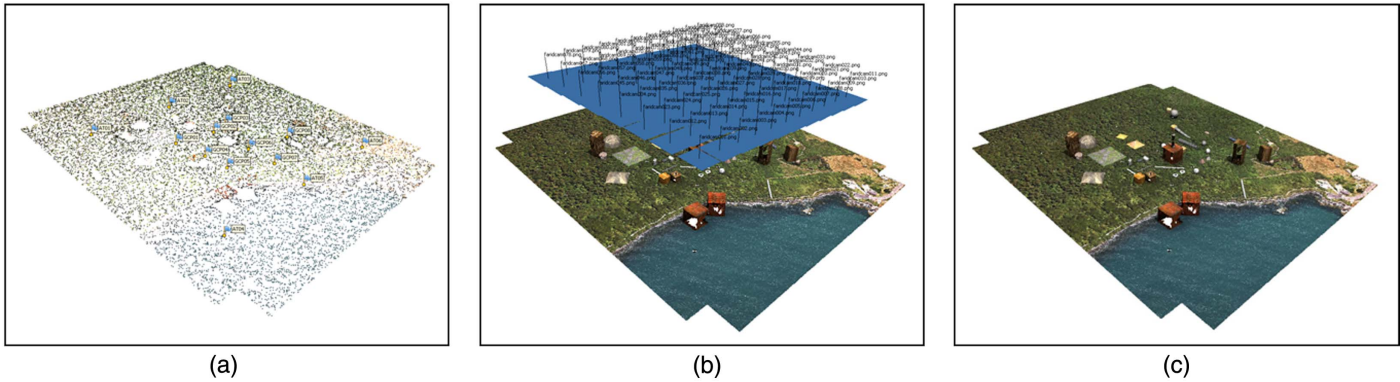


Fig. 7. (a) Resultant sparse point cloud; (b) dense point clouds with the camera locations and orientations; and (c) dense point clouds reconstructed for Simulation A3.

Table 1. General information of SfM-MVS processing and resultant point cloud for scenarios of simulation Scenes A and B

| Simulation | Attribute | 1 | 2 | 3 | 4 | 5 |
|------------|--------------------------|--------------------|--------------------|--------------------|--------------------|--------------------|
| A | No. of points, sparse | 25.8×10^3 | 25.5×10^3 | 25.1×10^3 | 24.8×10^3 | 25.0×10^3 |
| | RMSE _{GCP} (mm) | 0.05 | 0.03 | 0.02 | 0.05 | 0.06 |
| | RMSE _{CP} (mm) | 2.0 | 1.9 | 1.9 | 1.8 | 1.8 |
| | No. of points, dense | 9.5×10^6 | 9.7×10^6 | 9.4×10^6 | 9.4×10^6 | 9.2×10^6 |
| B | No. of points, sparse | 28.9×10^3 | 26.7×10^3 | 26.0×10^3 | 25.6×10^3 | 25.4×10^3 |
| | RMSE _{GCP} (mm) | 0.09 | 0.03 | 0.04 | 0.06 | 0.03 |
| | RMSE _{CP} (mm) | 2.0 | 2.0 | 1.8 | 1.9 | 1.9 |
| | No. of points, dense | 9.9×10^6 | 10.2×10^6 | 9.6×10^6 | 10.2×10^6 | 9.2×10^6 |

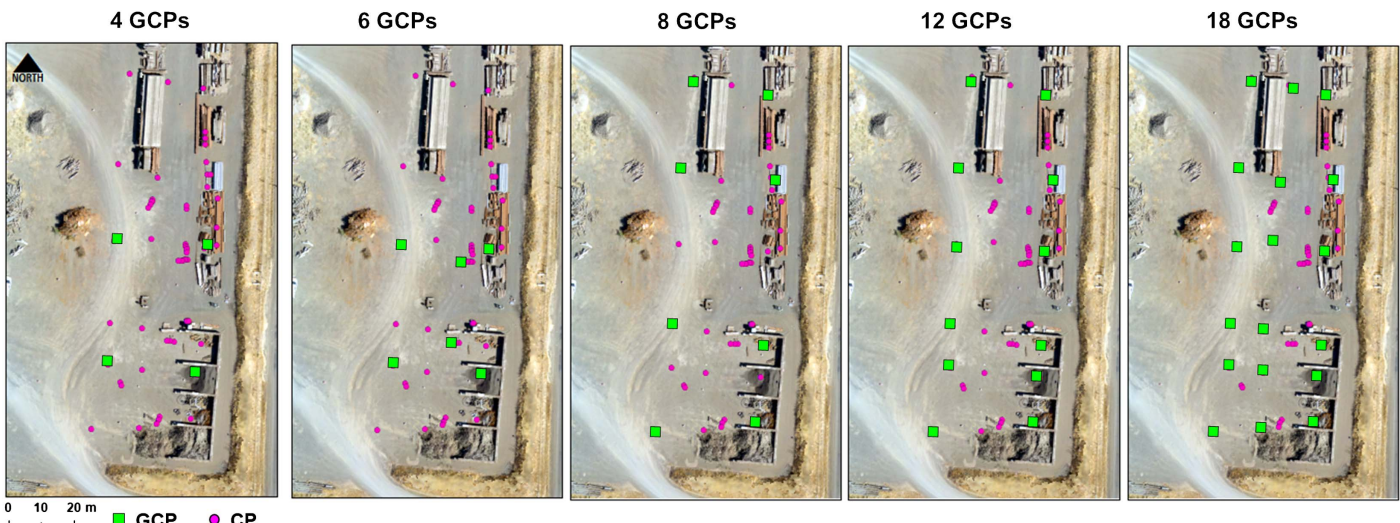


Fig. 8. Overview of GCPs selection for scenarios of empirical data set.

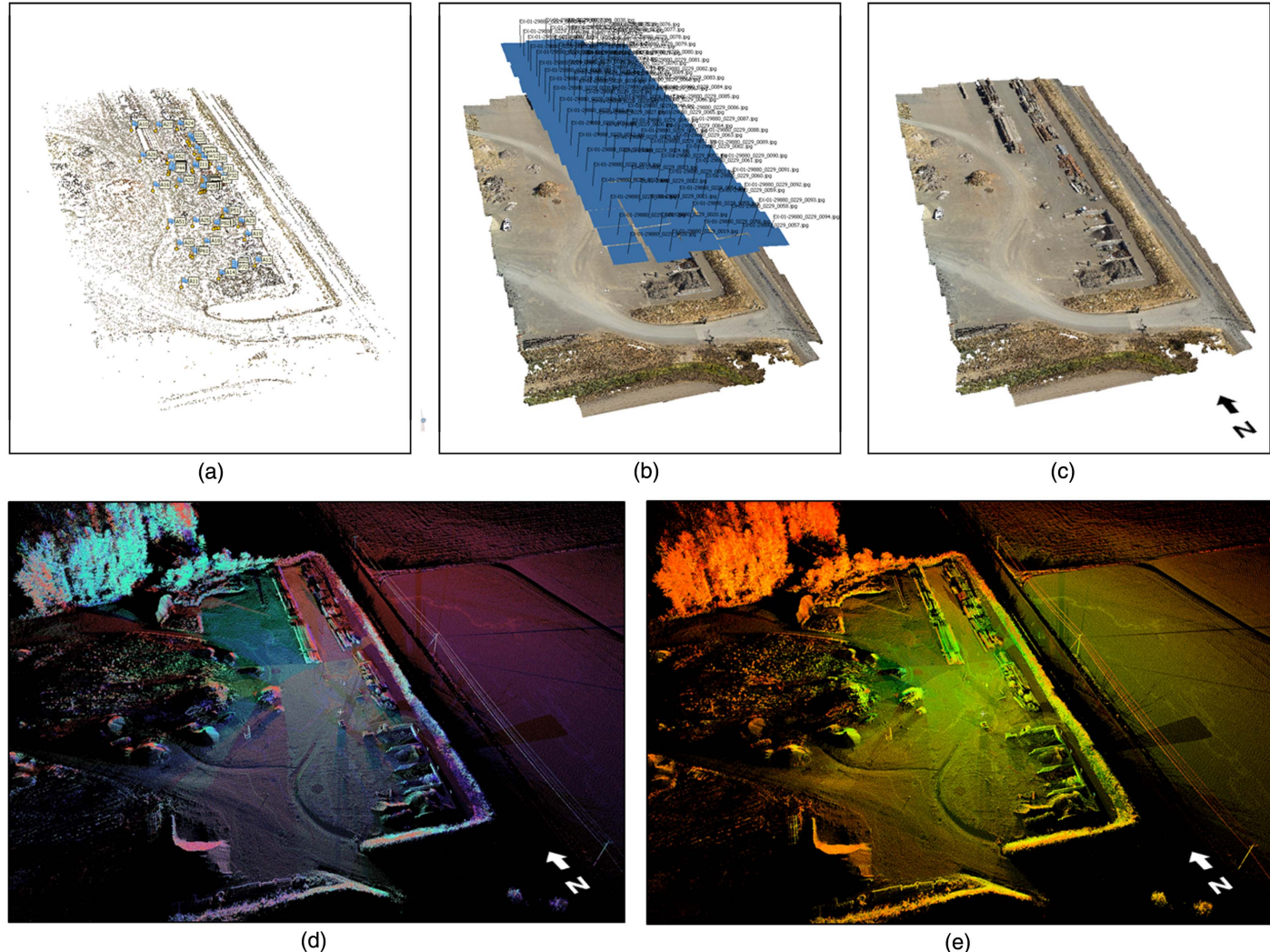
targets and using the rest of the aerial targets and/or markings and CPs. For each iteration, the subsets of GCPs were selected so as to evenly spread them throughout the scene as much as was practical. The layouts of GCPs and CPs for the scenarios of the empirical data set are shown in Fig. 8. The total error of GCPs and CPs is reported in Table 2.

The final dense point cloud was processed using high-quality and mild depth-filtering settings. The total processing time to generate a dense point cloud was 1 h for each scenario. The results for the scenario with 18 GCPs are shown in Figs. 9(a–c). The resultant

coordinates from LSA also were used to register the lidar data set to the same coordinates as the SfM data. All six scans were coregistered by constraining the clouds to the extracted targets and cloud-to-cloud registration in Cyclone version 9.1 [Figs. 9(d and e)]. The registration resulted in a 3D RMSE of 1.4 and 1.5 cm for target-only and for target and cloud-to-cloud (C2C) constraints, respectively. The composite point cloud of all scans contained 101 million points within the study area. The lidar point clouds were resampled to a minimum space between points of 2 cm to increase the processing speed; then the lidar point cloud was cropped to the area with

Table 2. General information of SfM-MVS processing and resultant point cloud for empirical data

| No GCPs | 4 | 6 | 8 | 12 | 18 |
|-------------------------|--------------------|--------------------|--------------------|--------------------|--------------------|
| No. of CPs | 52 | 50 | 48 | 44 | 38 |
| RMSE _{GCP} (m) | 0.004 | 0.009 | 0.011 | 0.012 | 0.013 |
| RMSE _{CP} (m) | 0.058 | 0.028 | 0.024 | 0.016 | 0.016 |
| No. of points, sparse | 5.5×10^3 |
| No. of points, dense | 84.6×10^6 | 84.6×10^6 | 84.6×10^6 | 84.4×10^6 | 84.4×10^6 |

**Fig. 9.** (a) Resultant sparse point clouds; (b) dense point clouds and camera locations and orientations; (c) dense point clouds reconstructed for 18-GCP scenario; (d) lidar point clouds shaded differently for each scanner; and (e) intensity-shaded lidar point clouds.

existing SfM-MVS dense point clouds to avoid miscalculation of the absolute 3D cloud-to-cloud distance (L_{C2C}) for points out of the SfM model. The resampled and cropped point clouds included about 14.2 million points (Table 3).

3D Reconstruction Error

The 3D reconstruction error (e) was defined by comparing the SfM-MVS dense point cloud with a ground truth model. The error was calculated as the L_{C2C} of points in ground truth data from the closest point in the SfM point cloud. Lague et al. (2013) gave more information about approaches to 3D cloud-to-cloud comparison by calculating the closest point distance. Lidar was used as the ground truth model of the empirical data, and the 3D geometry model was

used as the ground truth model for the simulated data. The simulated geometry was exported as a Wavefront obj file, and then the obj model was resampled with 10 million points in open-source software CloudCompare.

Table 3. General information of lidar for empirical data set

| Attribute | Value |
|---------------------------|---------------------|
| No. of scans | 6 |
| No. of targets | 21 |
| RMSE, targets (cm) | 1.4 |
| RMSE, target and C2C (cm) | 1.5 |
| No. of points | 101.1×10^6 |

Dense Point Cloud Quality Factors

This section describes the DPQF and the calculations. The estimated quality indexes are added as new attributes to the points in addition to the traditional x , y , z , and color values of the dense point cloud.

Distance to Keypoint Features

Distance to keypoint features (d_{kp}) was defined as the distance of a point in the dense point cloud from the closest point in the sparse point cloud, which can be calculated by comparing the two clouds. For the data sets, d_{kp} was calculated as L_{C2C} between the dense point cloud and the sparse point cloud in CloudCompare.

Distance to GCP

For each point in the dense point cloud, distance to GCP (d_{gcp}) was the distance to the closest GCP used in georeferencing of the SfM models. The coordinates of the GCPs were imported to CloudCompare, and the L_{C2C} between the dense point cloud and GCPs were calculated.

Angle of Incidence

The angle of incidence (α_{inc}) is described as the angle between the surface normal at the point P and the line from the camera center C to the point using

$$\alpha_{inc} = \tan^{-1} \left(\frac{\|\vec{\mathbf{N}}_P \times \vec{\mathbf{u}}_{CP}\|}{\vec{\mathbf{N}}_P \cdot \vec{\mathbf{u}}_{CP}} \right) \quad (1)$$

where $\vec{\mathbf{N}}_P$ = surface normal vector at point; and $\vec{\mathbf{u}}_{CP}$ = unit vector between point and camera, which is calculated using their position vectors

$$\vec{\mathbf{u}}_{CP} = \frac{1}{\|\vec{\mathbf{r}}_P - \vec{\mathbf{r}}_C\|} (\vec{\mathbf{r}}_P - \vec{\mathbf{r}}_C) \quad (2)$$

The point normal vectors were estimated by fitting quadratic surfaces to the neighboring points (OuYang and Feng 2005) in the $+z$ orientation, and the camera positions were obtained from the estimated camera EO from the SfM solution. Due to image overlap, each point was viewed from multiple cameras, and the average of the incidence angle to each of these cameras was computed as an attribute for each point. If all the cameras are pointing in a particular direction, for example, in vertical (nadir) photogrammetry, it is possible to use the $-z$ unit vector $(0, 0, -1)$ and calculate only the angle of the surface (α_{sur}) instead of the angle of incidence.

Camera Stand-Off Distances

The camera stand-off distances (d_c), or the distances between the point P in the dense point cloud and the camera, were calculated using their 3D coordinates [Eq. (3)], then the average distance between the point and all camera are assigned as a new attribute to the point

$$d_c = \|\vec{\mathbf{r}}_C - \vec{\mathbf{r}}_P\| \quad (3)$$

Number of Images

The number of images (n_{img}) used for the 3D reconstruction in a SfM-MVS solution can be estimated by using the IO and EO parameters obtained from SfM together with the real-world coordinate transformation parameters, from which it is possible to back-calculate the 2D pixel coordinates of every 3D point in the scene. For each point, if the 2D coordinates are located in the image, the counter is augmented by 1, and the final counter value of the number of images is attributed to the point in the cloud. This approach lacks the ability to deal with occlusions; this problem is addressed

by considering the angles of incidence. The point is considered to be seen in the image if the angle of incidence is less than 90° . This criterion filters points that are on surfaces that do not face the camera if their pixel coordinates are within the image plane. Future developments can incorporate more-advanced ray-tracking analysis in the number of image calculations. For this study, there was minimal occlusion in the scene. Hence the effect of those occlusions on the DPQFs was determined to be negligible.

Brightness and Darkness Indexes

Brightness (I_b) and darkness (I_d) of a point can be related to its color value from the overlapping images that include the reconstructed point. The estimated color may have a series of color balancing or averaging depending on the methodology used in the SfM-MVS approach. This study used the red-green-blue (RGB) color values from the final point cloud to define the brightness and darkness factors. The RGB values then were converted to a normalized grayscale intensity value between -1 and 1 [Eq. (4)] (Anderson et al. 1996), and the brightness and darkness indexes were calculated for each point using

$$\tilde{I}_{gray} = \frac{2 \times (0.2126 \times R + 0.7152 \times G + 0.0722 \times B)}{255} - 1 \quad (4)$$

$$I_b = \tilde{I}_{gray}, I_d = 0 \quad \tilde{I}_{gray} > 0 \quad I_d = \tilde{I}_{gray}, I_b = 0 \quad \tilde{I}_{gray} < 0 \quad (5)$$

Results and Discussion

Fig. 10 shows the ground truth models [Figs. 10(a and e)], SfM-MVS dense point clouds [Figs. 10(b and f)], and the calculated 3D error for sections of Scene A3 of the simulated [Fig. 10(c)] and the empirical data sets [Fig. 10(g)]. In addition, a profile view of a box in the simulated data [Fig. 10(d)] and a pipe in the empirical data [Fig. 10(h)] are shown, and the L_{C2C} calculations are schematically illustrated. Figs. 11 and 12 show the maps of error and the DPQF indexes including, keypoint features distribution d_{kp} , GCP distribution d_{gcp} , scene geometry α_{sur} (representing the angle of incidence), camera stand-off distances d_c , image coverage n_{img} , brightness index I_b and darkness index I_d for a simulated scene (A3 scenario) and an empirical data set (6-GCP scenario).

To better visualize the variations of DPQF with respect to changes of lighting conditions, the simulated model and the SfM-MVS point clouds for all five scenarios of Scene A are shown in Fig. 13. Changing the lighting conditions from Scenarios A1 to A5 impacted a number of DPQFs, including d_{kp} , I_b , and I_d (Fig. 13). When estimating the DPQF, there were no variations in the d_{gcp} and α_{sur} indexes because they are independent of changes in lighting conditions. In addition, the factors depending on the locations of cameras, (i.e., d_c and n_{img}) were minimally impacted within the simulated scenarios because the locations of the cameras were not changed from scenario to scenario.

The lighting condition had a distinguishable impact on the error in scenes (Fig. 13). For example, the 3D error visualizations show that changing the lighting conditions from Scenario A1 to A2, which created stronger shadows (lower ambient light), resulted in data gaps on the vertical faces. There was less error in Scenario A3 than in Scenarios A1 and A2 because its sun and ambient light intensity values reduced the amount of shadow. Increasing the sun-light intensity in Simulation A5 improved the quality of reconstruction on the shadowed faces of boxes; however, at the same time, it adversely impacted the reconstruction quality on the brighter

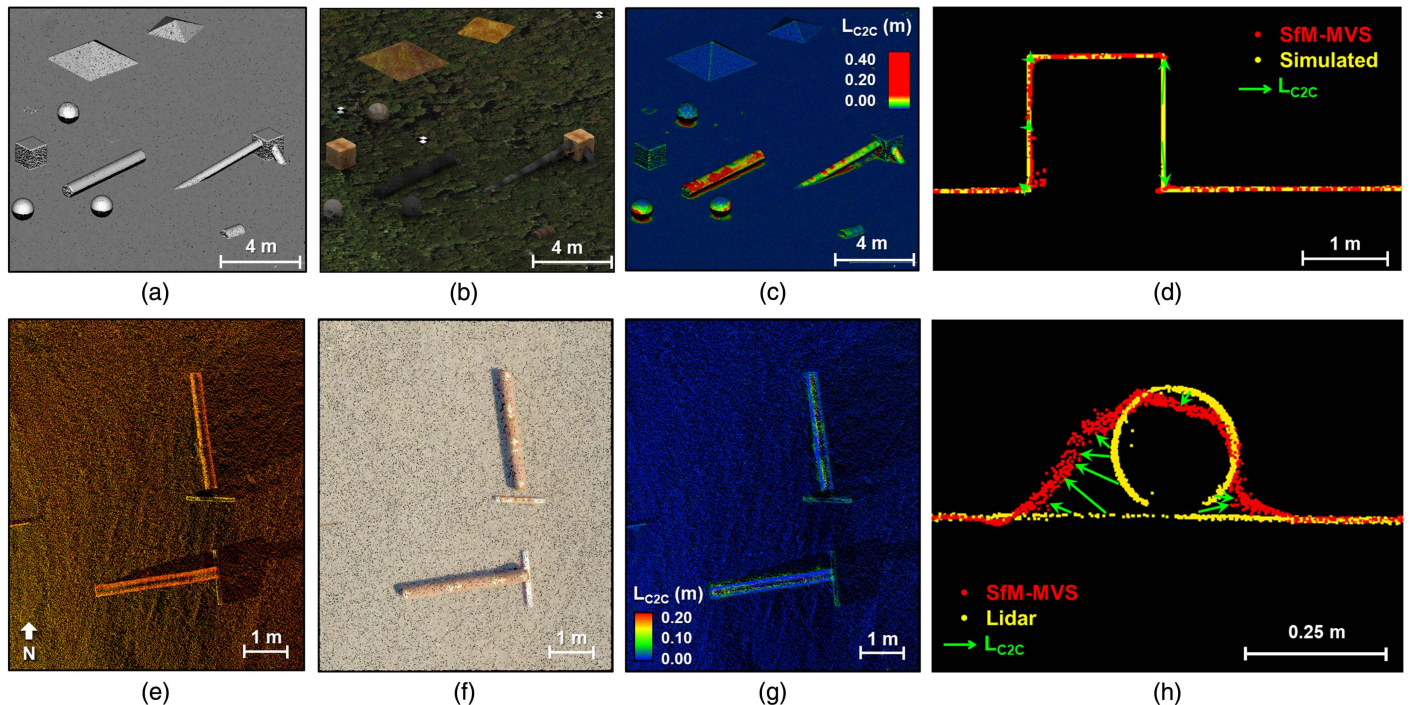


Fig. 10. (a) Ground truth model for a part of Scenario A3; (b) SfM-MVS dense point cloud for Scenario A3; (c) 3D error for Scenario A3; (d) profile view of the SfM-MVS and ground truth point clouds and schematic 3D error calculation for Scenario A3; (e) lidar point cloud for a section of Langmack data set with 18 GCPs; (f) SfM-MVS dense point cloud for a section of Langmack data set with 18 GCPs; (g) 3D error for a section of Langmack data set with 18 GCPs; and (h) profile view of SfM-MVS and ground truth point clouds and schematic 3D error calculation for a section of Langmack data set with 18 GCPs.

or shiny surfaces, such as the top of the pipes and the bright textured pyramids in 3D error visualizations for A5. The reason for the poor reconstruction on light surfaces is that the excess of light masked features and minimized the sparse point cloud density. Moreover, there was not enough texture to perform further matching and expanding between sparse points in the densification step. As a result, data gaps and a reconstruction occurred in these overexposed regions. However, it appeared that this was not the case for areas on the flat ground surface, where areas with higher brightness index still had proper 3D reconstruction from the images. This might be because of the better performance of SfM-MVS on the flat ground surface, which can be seen in both the experimental and the simulated data sets.

For the empirical data, Fig. 14 shows the spatial distribution of the error in SfM-MVS point clouds of the Langmack area for scenarios with different numbers of GCPs. As expected, having the appropriate number of GCPs was essential for processing the empirical data set, and the amount of error and its distribution significantly were controlled by the GCPs. For this data set, the accuracy of 3D reconstruction considerably improved for scenarios with eight or more GCPs. For the simulation data set, the number of GCPs did not appear to be a significant factor. This result was expected for the simulated data because the locations of the cameras were known and were provided to the software, and the camera calibration model was accurately defined. However, for the empirical data set, the impact was significant mainly because an uncalibrated camera was used, with unknown or less accurately known lens distortion parameters and low-accuracy EO positions. In addition to the error for scenarios with a limited number of GCPs, some points were mapped continuously as erroneous points. The points mostly were in areas with high vegetation, at the borders of the study area, as well as

those with piles of biomass, located in the center of the study area. The problem with these points is that there was no well-defined surface to capture with lidar, and the lidar pulse can be from either outer or inner objects. Therefore, the ground truth lidar data for these regions are not reliable, and it is not expected that a SfM dense point cloud could be built that reproduced the same results. In addition, there were significant errors for spaces between the concrete bridge objects, where there were no data in the SfM data set, but TLS was able to capture the geometry. The errors resulted from covered objects, and the error on vegetation is not meant to be included in the future analysis, so the regions with vegetation and biomass were cropped out for the final data, and the points with error larger than 21.7 cm were omitted from further analysis. The cut-off of 21.7 cm was determined based on the RMSE of total 3D error for cropped data of the scenario with the smallest error ($1.6166 \times \text{RMSE3D}$), also based on the performance of selected cut-off in filtering the points with an error.

The total RMSE of the 3D reconstruction error based on C2C distances for each simulated scenario is shown in Fig. 15(a). Both underexposed scenes (A1, A2, B1, and B2) and overexposed scenes (A5 and B5) had higher reconstruction error. This error appeared to be even higher for the overexposed situation. Scenes with minimal shadow effect (A3 and B3) and with balanced sun and ambient light conditions (A4 and B4) had fewer errors.

The RMSE for cropped and filtered empirical data, the georeferencing error, and the RMSE of CP error are shown in Fig. 15(b). The error was highest with four GCPs, and it decreased as more GCPs were used for georeferencing. The change of the RMSE of CPs followed the same trend but with smaller values. This difference was expected because the RMSE represents only selected CPs in the model that usually exist in the sparse point cloud. In most

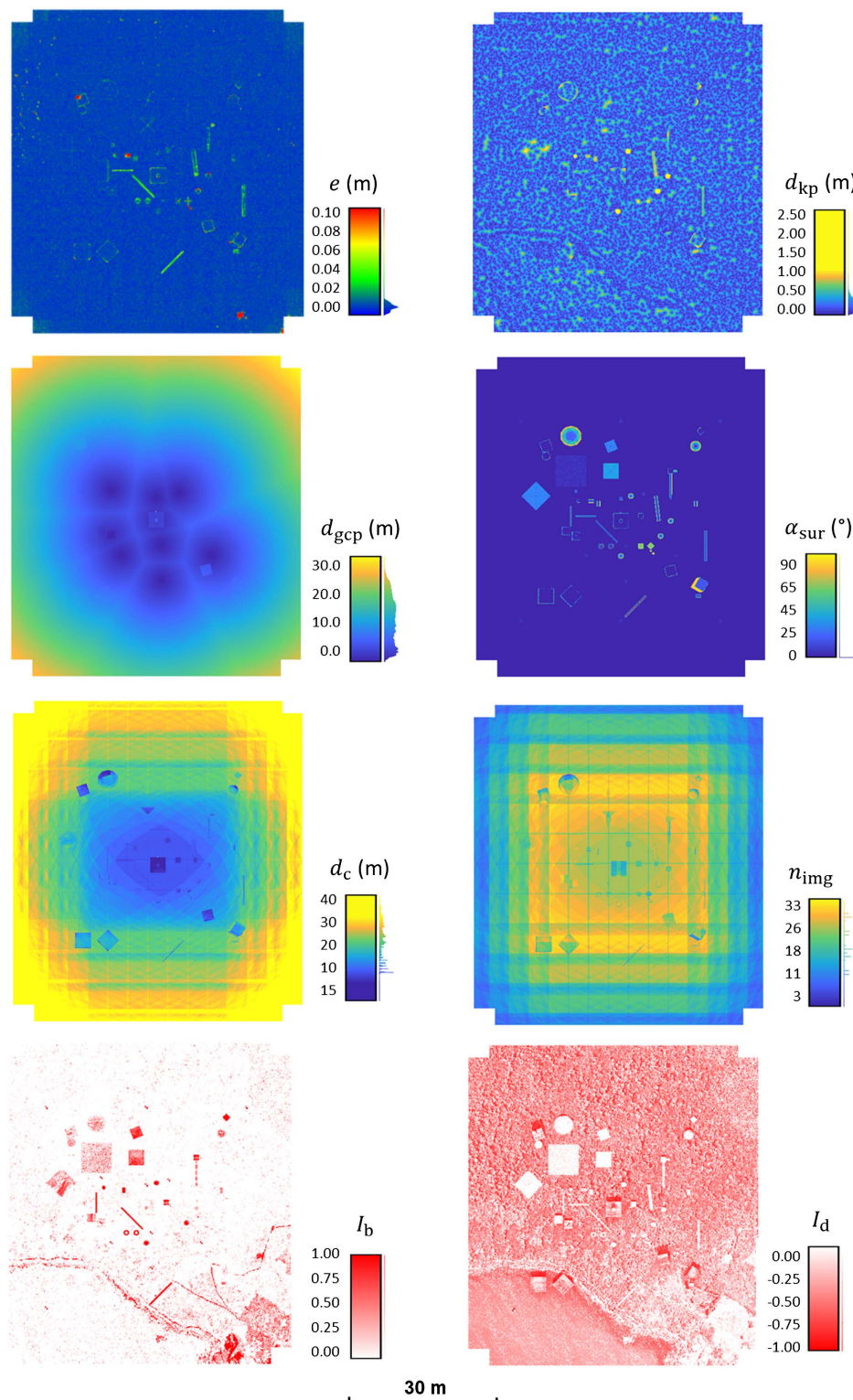


Fig. 11. DPQFs for Scenario A4 of the simulated data set.

cases, the CPs are distinct objects in the scene creating key point features that can be extracted and used in sparse point clouds, which have more-confident 3D construction. The regions near high-contrast markings can help to generate results that are more accurate at those locales; however, smooth and featureless regions might have a higher error. This study shows that comparing the SfM-MVS-modeled coordinates of CPs and comparing the accurately measured CPs can be a relatively good representation of the overall

accuracy of the sparse point cloud; however, higher error should be expected in dense point clouds. Interestingly, the RMSE of georeferencing increases as more GCPs are included in the processing. The reported RMSE for georeferencing error must be handled with care. This error might be due to errors in GCP coordinates. The error also might increase as more constraints are added to the least-squares solution for coordinate transformation by providing a more realistic estimation of georeferencing error.

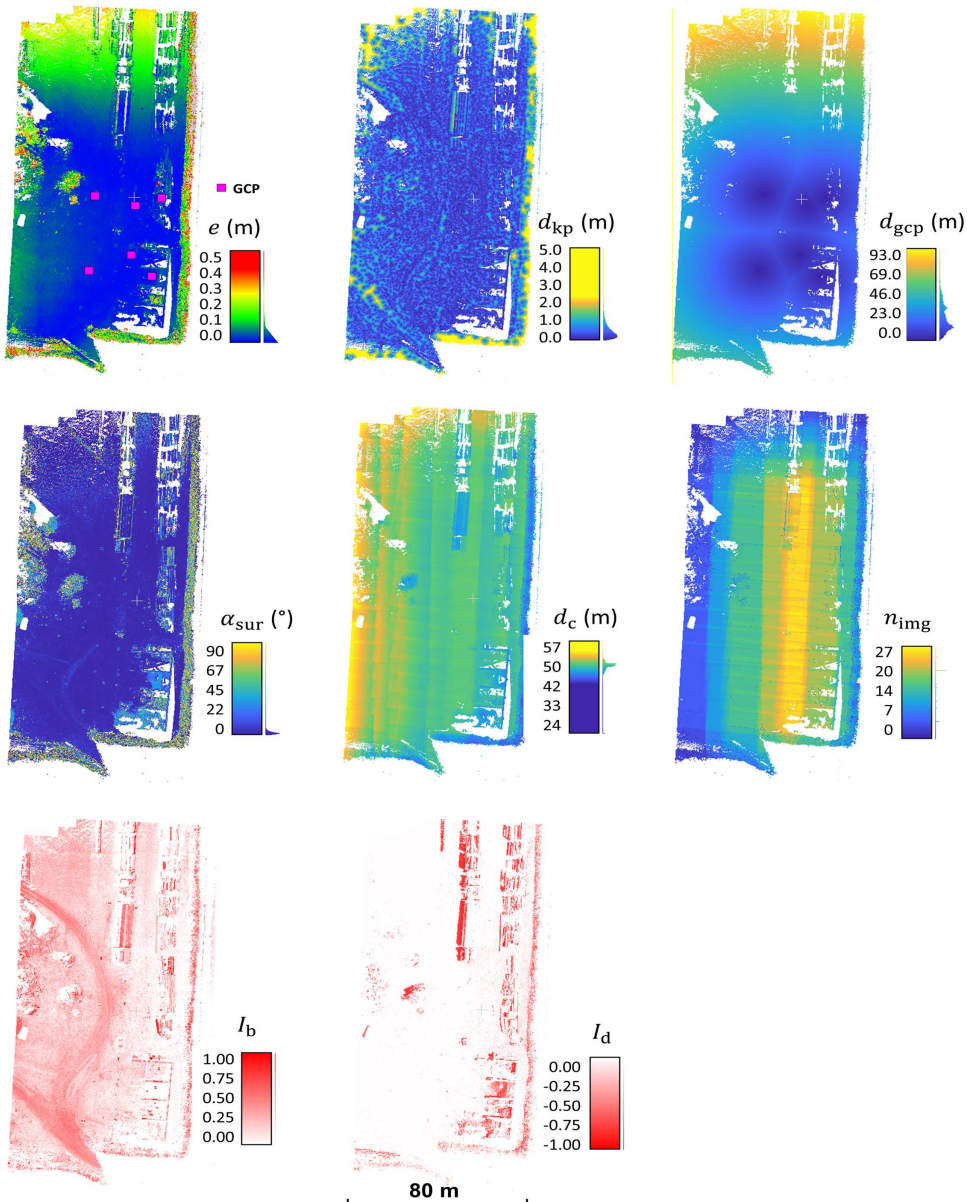


Fig. 12. DPQFs for the scenario with six GCPs for Langmack empirical data set.

One objective of this study was to investigate the correlations of the aforementioned quality factors with the error. In addition, to study the relation of each factor to reconstruction error, the statistical relationships between the DPQFs were calculated by developing the Pearson correlation matrices for each scenario. The correlation coefficients are between -1 and 1 . The closer the coefficient is to either -1 or 1 , the stronger is the linear dependency between the variables, and a value of 0 implies that the variables are independent. The correlation coefficient matrices of the simulated scenarios are shown in Fig. 16. The red and blue colors indicate the positive and negative correlation, respectively, where the darker colors stand for greater correlations of each, and the white color indicates no correlation between variables.

In almost all A and B simulations, there was higher correlation between error and d_{kp} and α_{sur} factors, with coefficients of 0.4 – 0.5 . This correlation pattern appeared to be similar in all simulations, indicating that most of the error occurred on near-vertical surfaces or locations far from the keypoint features. The d_{kp} and α_{sur} also had higher intercorrelation, indicating that the density of the sparse

point cloud was lower on vertical surfaces with a high angle of incidence. The correlation between I_d and α_{sur} was highest for Scenarios A5 and B5, in which, because of the lighting condition, darker points existed mostly in the shadowed regions. Interestingly, there was a positive correlation between I_b and I_d , whereas these factors were expected to be negatively correlated. This correlation was due to the definition of these factors, because for most of the points the I_b and I_d were small, with a normalized grayscale value close to zero. This normalized value was assigned to I_b and I_d whether the value was slightly positive or negative, and the other factor was assigned zero value. Low values of one index close to zero and a value of zero for the other index result in high correlation between them. The high 0.90 correlation coefficient between d_c and d_{gcp} or the -0.60 coefficient between d_{gcp} and n_{img} resulted merely because of the geometry of the scene, in which all the GCPs were located at the center of the scene, with more image coverage and a closer distance from the cameras.

The correlation matrices of Langmack data for scenarios with a different number of GCPs are presented in Fig. 17. Supporting the

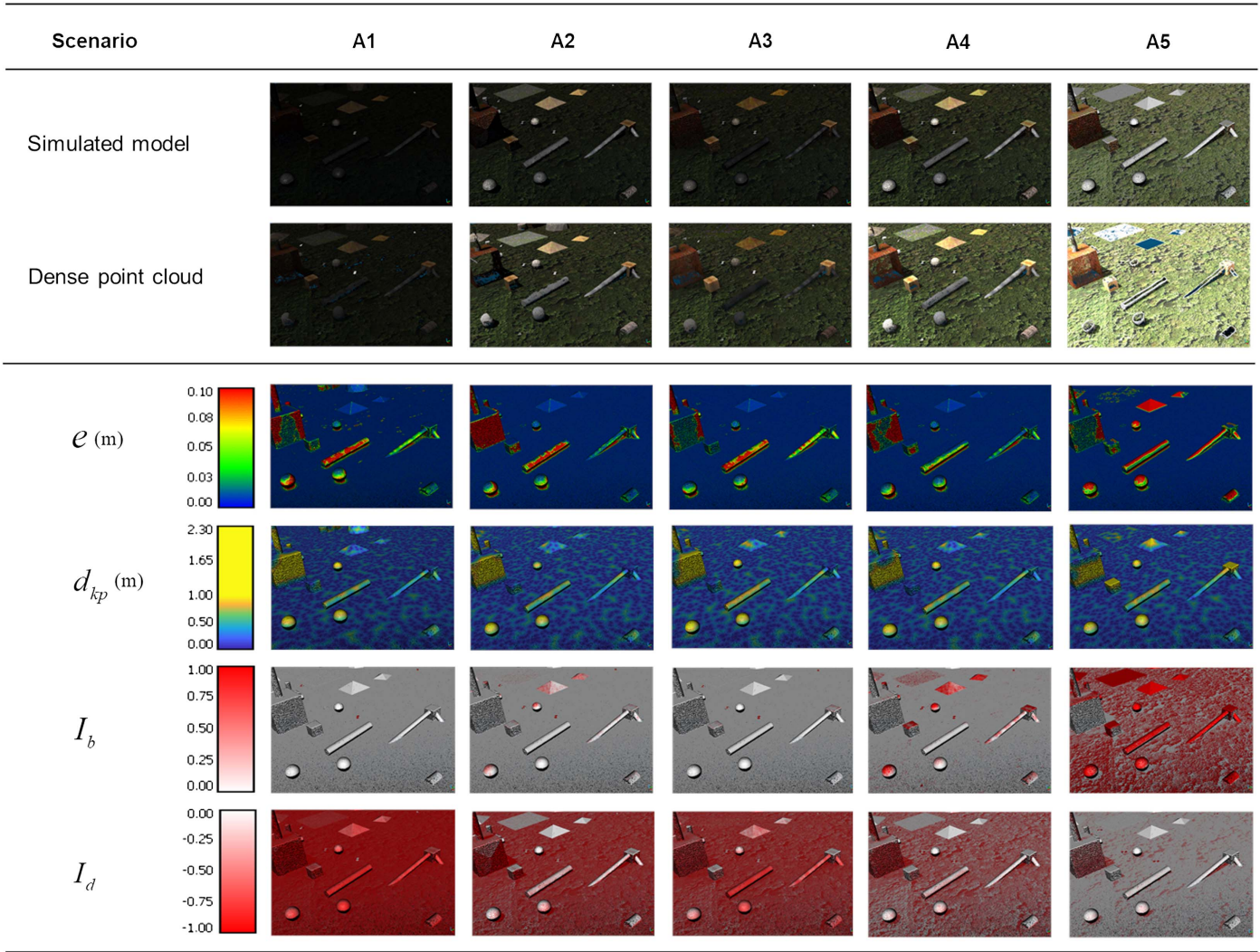


Fig. 13. Change of DPQFs for scenario of simulated Scene A.

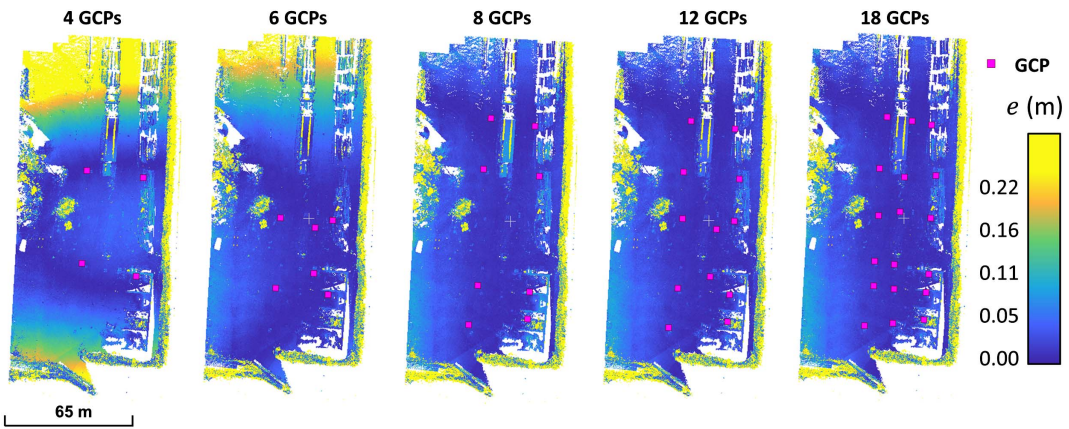


Fig. 14. Changes in the spatial distribution of 3D error with respect to the changes in the number of GCPs.

trend and pattern of error in Figs. 14 and 15(b), there was a high correlation coefficient of 0.65 between e and d_{gcp} for scenarios with four and six GCPs, showing that points with higher error were located at greater distance from GCPs. The results suggest that adding more GCPs significantly improved the quality of the SfM result;

however, the improvement plateaued after eight GCPs at this site. Furthermore, improving the accuracy by adding GCPs decreased the correlation coefficients of error and d_{gcp} . The number of GCPs is site-specific, and heavily depends on the size of the area, terrain complexity, texture richness, and distribution of GCPs.

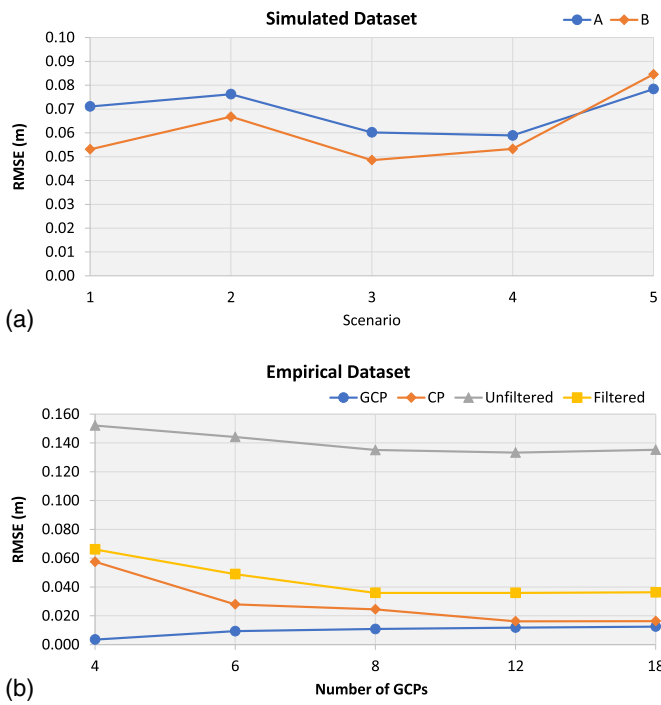


Fig. 15. (a) RMS of 3D error for all scenarios of A and B simulations; and (b) RMS of georeferencing error, CP error, and 3D error for non-filtered and filtered point clouds of Langmack data set.

Figs. 18(a and b) graphically represent the correlation coefficients between e and the DPQFs for Scenes A and B, respectively. The coefficients were similar in most of the scenes, with high correlations between the error with d_{kp} and α_{sur} variables. This correlation coefficient would change if the simulation were adjusted by adding oblique images that capture the vertical surfaces, which were not captured in nadir images to improve the construction quality. In that case, the correlation between error and α_{sur} (or α_{inc} for the case of oblique and nadir imagery) could decrease. It then would be possible to analyze the correlation of the other factors that are overlaid by the more significant error at a greater distance from the keypoint features at vertical surfaces. The correlation coefficients between e and DPQFs are shown in Fig. 18(c). For scenarios with more GCPs, the error became more independent of distance to a GCP. The remainder of the error had higher correlation coefficients with n_{img} , α_{sur} , and I_d . The n_{img} factor also was correlated with d_{gcp} for scenarios with 12 and 18 GCPs, because more GCPs were located in the center of the area with a higher number of images. Furthermore, the correlation between α_{sur} and d_c resulted from the site setup, because the center of the study area, which was closer to the cameras, was flat, and different objects that created α_{sur} were located around the edges of the area. However, I_d and α_{sur} had a meaningful correlation, whereas points with I_d values closer to -1 were located on vertical faces or overhanging surfaces, which mostly were in shaded areas.

Best Practices for UAS Surveys

Keypoint Features

The sparse point cloud formed from keypoints is the backbone of the current image-based reconstruction techniques. The dense cloud is recovered by matching and expanding between sparse points. Higher error is expected if there are not sufficient keypoints.

A low-density sparse point cloud can result from object surface characteristics, sensor quality, blurred images, camera range, camera exposure, and processing method, some of which can be improved by proper data capture and processing practices.

GCPs

An appropriate number of GCPs is essential for processing uncalibrated camera with unknown or inaccurate known camera parameters. This number heavily depends on the size of the area, terrain, GCP distribution, and image network geometry. Bolkas (2019), Chudley et al. (2019), Rangel et al. (2018), Sanz-Ablanedo et al. (2018), and references therein provided in-depth discussion.

Angle of Incidence

A large angle of incidence appears to result in greater error. In other words, SfM cannot properly recover a scene if it is not properly captured in images. Usually, adding oblique imagery can assist with complete 3D capture of objects to recover vertical surfaces, e.g., building facades. There should be enough overlap between vertical and oblique image sets to ensure strong image network interconnection.

Camera Stand-Off Distance

In the sample data set, the stand-off distances did not appear to be significant due to a low elevation variation range. However, in combination with sensor and lens characteristics, camera stand-off is important for flight height planning based on ground sampling distance requirements that can be related to designed accuracy (Cali and Ambu 2018; González-Quiñones et al. 2018).

Number of Images

The number of images or the amount of overlap is an import requirement for SfM/MVS processing. Based on observations at the outer edges of the sample data sets, a minimum redundancy of three images and a strong image network are needed to ensure reliable reconstruction of a point.

Brightness and Darkness

Shadow can degrade the quality of the SfM-MVS point cloud. Point cloud densification is vulnerable in featureless and nontextured regions such as strong shadow. An environment with balanced ambient and direct light is preferred for UAS surveys (e.g., a bright cloudy day). Shadows are shortest but strongest at noon, so data taken during this time may have less shadow; however, the 3D reconstruction can be poor in that situation. Like shadow, very bright objects also can degrade the quality. Using HDR imaging technology or taking additional images with adjusted camera exposure can improve the quality. Discussion of the technical complications of using such techniques from fast-moving UAS platforms is beyond the scope of this manuscript.

Conclusions and Future Works

This paper defines quality factor indexes to be used as proxy indicators for assessing the accuracy of SfM-MVS dense point clouds. The dense point cloud quality factors include distance to GCPs, distance to keypoint features, number of images, distance to cameras, angle of incidence, brightness index, and darkness index. Simulated and empirical experiments were used to assess the accuracy of image-based 3D reconstructed models with respect to different data collection and site conditions. The data were used to estimate the DPQFs that reflected the scenarios settings, then the spatial correlation between the DPQFs and the reconstruction error was investigated for multiple data sets.

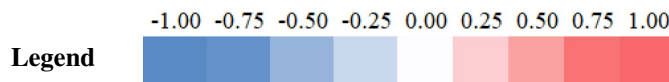
| A1 | d_{kp} | d_{gcp} | d_{img} | α_{sur} | d_c | I_b | I_d |
|----------------|----------|-----------|-----------|----------------|---------|---------|---------|
| e | 0.4983 | -0.1219 | -0.1342 | 0.5103 | -0.1598 | -0.0021 | -0.1018 |
| d_{kp} | | -0.1696 | -0.1882 | 0.6222 | -0.2270 | -0.0101 | -0.1730 |
| d_{gcp} | | | -0.6074 | -0.2668 | 0.8898 | -0.0251 | 0.0222 |
| d_{img} | | | | -0.2693 | -0.5050 | 0.0144 | 0.0264 |
| α_{sur} | | | | | -0.3490 | -0.0027 | -0.1516 |
| d_c | | | | | | -0.0177 | 0.0819 |
| I_b | | | | | | | 0.2958 |

| A2 | d_{kp} | d_{gcp} | d_{img} | α_{sur} | d_c | I_b | I_d |
|----------------|----------|-----------|-----------|----------------|---------|---------|---------|
| e | 0.4924 | -0.1351 | -0.1481 | 0.5029 | -0.1688 | -0.0102 | -0.1561 |
| d_{kp} | | -0.1717 | -0.1881 | 0.6434 | -0.2203 | 0.0065 | -0.2182 |
| d_{gcp} | | | -0.6074 | -0.2668 | 0.8898 | -0.0598 | -0.0141 |
| d_{img} | | | | -0.2693 | -0.5050 | 0.0429 | 0.1065 |
| α_{sur} | | | | | -0.3490 | 0.0358 | -0.2117 |
| d_c | | | | | | -0.0514 | 0.0473 |
| I_b | | | | | | | 0.3386 |

| A3 | d_{kp} | d_{gcp} | d_{img} | α_{sur} | d_c | I_b | I_d |
|----------------|----------|-----------|-----------|----------------|---------|---------|---------|
| e | 0.4498 | -0.1080 | -0.1006 | 0.4647 | -0.1328 | -0.0084 | -0.0850 |
| d_{kp} | | -0.1957 | -0.1655 | 0.6246 | -0.2484 | -0.0304 | -0.1543 |
| d_{gcp} | | | -0.6075 | -0.2668 | 0.8898 | 0.0094 | 0.0989 |
| d_{img} | | | | -0.2691 | -0.5053 | -0.0167 | -0.0760 |
| α_{sur} | | | | | -0.3488 | -0.0156 | -0.1385 |
| d_c | | | | | | 0.0258 | 0.1604 |
| I_b | | | | | | | 0.2687 |

| A4 | d_{kp} | d_{gcp} | d_{img} | α_{sur} | d_c | I_b | I_d |
|----------------|----------|-----------|-----------|----------------|---------|---------|---------|
| e | 0.4421 | -0.1100 | -0.1053 | 0.4554 | -0.1277 | -0.0232 | -0.1810 |
| d_{kp} | | -0.1786 | -0.1714 | 0.6210 | -0.2326 | -0.0407 | -0.2340 |
| d_{gcp} | | | -0.6075 | -0.2670 | 0.8898 | -0.0216 | 0.0671 |
| d_{img} | | | | -0.2691 | -0.5053 | 0.0003 | 0.0465 |
| α_{sur} | | | | | -0.3490 | -0.0064 | -0.2681 |
| d_c | | | | | | 0.0202 | 0.1320 |
| I_b | | | | | | | 0.4348 |

| A5 | d_{kp} | d_{gcp} | d_{img} | α_{sur} | d_c | I_b | I_d |
|----------------|----------|-----------|-----------|----------------|---------|---------|---------|
| e | 0.3849 | -0.1034 | -0.0074 | 0.3305 | -0.1335 | 0.0031 | -0.1341 |
| d_{kp} | | -0.1857 | -0.1598 | 0.6148 | -0.2339 | -0.1083 | -0.2977 |
| d_{gcp} | | | -0.6074 | -0.2668 | 0.8898 | 0.0697 | 0.1487 |
| d_{img} | | | | -0.2693 | -0.5050 | 0.0358 | 0.0876 |
| α_{sur} | | | | | -0.3490 | -0.2444 | -0.4619 |
| d_c | | | | | | 0.1336 | 0.1926 |
| I_b | | | | | | | 0.5737 |



| B1 | d_{kp} | d_{gcp} | d_{img} | α_{sur} | d_c | I_b | I_d |
|----------------|----------|-----------|-----------|----------------|---------|---------|---------|
| e | 0.4558 | -0.1186 | -0.0924 | 0.4241 | -0.1393 | -0.0013 | -0.1192 |
| d_{kp} | | -0.1697 | -0.1314 | 0.5216 | -0.2045 | -0.0132 | -0.1700 |
| d_{gcp} | | | -0.6075 | -0.2669 | 0.8898 | -0.0252 | 0.0238 |
| d_{img} | | | | -0.2691 | -0.5053 | 0.0144 | 0.0328 |
| α_{sur} | | | | | -0.3489 | -0.0024 | -0.1754 |
| d_c | | | | | | -0.0178 | 0.0953 |
| I_b | | | | | | | 0.4037 |

| B2 | d_{kp} | d_{gcp} | d_{img} | α_{sur} | d_c | I_b | I_d |
|----------------|----------|-----------|-----------|----------------|---------|---------|---------|
| e | 0.4788 | -0.1299 | -0.1283 | 0.4696 | -0.1590 | -0.0056 | -0.1751 |
| d_{kp} | | -0.1591 | -0.1639 | 0.5689 | -0.1941 | 0.0071 | -0.2165 |
| d_{gcp} | | | -0.6075 | -0.2669 | 0.8898 | -0.0861 | -0.0266 |
| d_{img} | | | | -0.2692 | -0.5053 | 0.0678 | 0.1302 |
| α_{sur} | | | | | -0.3489 | 0.0506 | -0.2252 |
| d_c | | | | | | -0.0862 | 0.0428 |
| I_b | | | | | | | 0.3762 |

| B3 | d_{kp} | d_{gcp} | d_{img} | α_{sur} | d_c | I_b | I_d |
|----------------|----------|-----------|-----------|----------------|---------|---------|---------|
| e | 0.3814 | -0.1178 | -0.0605 | 0.3848 | -0.1381 | -0.0017 | -0.1276 |
| d_{kp} | | -0.2194 | -0.0786 | 0.4873 | -0.2379 | -0.0173 | -0.0992 |
| d_{gcp} | | | -0.6075 | -0.2669 | 0.8898 | -0.0205 | 0.1292 |
| d_{img} | | | | -0.2692 | -0.5053 | 0.0122 | -0.1210 |
| α_{sur} | | | | | -0.3489 | -0.0014 | -0.1459 |
| d_c | | | | | | -0.0159 | 0.2110 |
| I_b | | | | | | | 0.2277 |

| B4 | d_{kp} | d_{gcp} | d_{img} | α_{sur} | d_c | I_b | I_d |
|----------------|----------|-----------|-----------|----------------|---------|---------|---------|
| e | 0.4298 | -0.1156 | -0.0770 | 0.4123 | -0.1300 | -0.0006 | -0.2172 |
| d_{kp} | | -0.2080 | -0.1038 | 0.5203 | -0.2362 | 0.0084 | -0.2261 |
| d_{gcp} | | | -0.6075 | -0.2669 | 0.8898 | -0.0807 | 0.0875 |
| d_{img} | | | | -0.2692 | -0.5053 | 0.0481 | 0.0324 |
| α_{sur} | | | | | -0.3489 | 0.0608 | -0.3153 |
| d_c | | | | | | -0.0759 | 0.1915 |
| I_b | | | | | | | 0.4323 |

| B5 | d_{kp} | d_{gcp} | d_{img} | α_{sur} | d_c | I_b | I_d |
|----------------|----------|-----------|-----------|----------------|---------|---------|---------|
| e | 0.3687 | -0.0711 | -0.0262 | 0.2565 | -0.0782 | 0.0835 | -0.1598 |
| d_{kp} | | -0.2401 | -0.0783 | 0.5211 | -0.2734 | -0.0762 | -0.3809 |
| d_{gcp} | | | -0.6075 | -0.2669 | 0.8898 | 0.0796 | 0.1972 |
| d_{img} | | | | -0.2691 | -0.5053 | 0.0115 | 0.1415 |
| α_{sur} | | | | | -0.3489 | -0.2747 | -0.6152 |
| d_c | | | | | | 0.2027 | 0.2244 |
| I_b | | | | | | | 0.4154 |

Fig. 16. Pearson correlation coefficients between DPQFs for Simulations A and B (matrices are symmetric).

| 4 GCP | d_{kp} | d_{gcp} | d_{img} | α_{sur} | d_c | I_b | I_d |
|----------------|----------|-----------|-----------|----------------|---------|---------|---------|
| e | 0.0917 | 0.6525 | -0.0948 | 0.0196 | 0.0849 | 0.0470 | -0.0698 |
| d_{kp} | | 0.1145 | -0.2521 | 0.0481 | 0.1269 | 0.0422 | -0.0791 |
| d_{gcp} | | | -0.2995 | 0.0178 | 0.3415 | 0.1421 | 0.0499 |
| d_{img} | | | | -0.2772 | -0.1927 | -0.2076 | 0.0500 |
| α_{sur} | | | | | -0.4291 | 0.0384 | -0.4612 |
| d_c | | | | | | 0.1702 | 0.2957 |
| I_b | | | | | | | 0.4111 |

| 8 GCP | d_{kp} | d_{gcp} | d_{img} | α_{sur} | d_c | I_b | I_d |
|----------------|----------|-----------|-----------|----------------|---------|---------|---------|
| e | 0.1545 | 0.1622 | -0.3302 | 0.3027 | -0.0047 | 0.0465 | -0.2893 |
| d_{kp} | | 0.1162 | -0.2578 | 0.0394 | 0.1266 | 0.0399 | -0.0760 |
| d_{gcp} | | | -0.3114 | -0.1069 | 0.4938 | 0.0901 | 0.1434 |
| d_{img} | | | | -0.2788 | -0.1762 | -0.2100 | 0.0433 |
| α_{sur} | | | | | -0.4333 | 0.0497 | -0.4453 |
| d_c | | | | | | 0.1590 | 0.2881 |
| I_b | | | | | | | 0.4040 |

| 18 GCP | d_{kp} | d_{gcp} | d_{img} | α_{sur} | d_c | I_b | I_d |
|----------------|----------|-----------|-----------|----------------|---------|---------|---------|
| e | 0.1762 | 0.3346 | -0.3958 | 0.2863 | 0.1124 | 0.0669 | -0.2747 |
| d_{kp} | | 0.2180 | -0.2600 | 0.0438 | 0.1242 | 0.0399 | -0.0770 |
| d_{gcp} | | | -0.6389 | -0.0658 | 0.5205 | 0.1370 | 0.1177 |
| d_{img} | | | | -0.2815 | -0.1742 | -0.2112 | 0.0458 |
| α_{sur} | | | | | -0.4333 | 0.0480 | -0.4508 |
| d_c | | | | | | 0.1623 | 0.2957 |
| I_b | | | | | | | 0.4057 |

Fig. 17. Pearson correlation coefficients between DPQFs all scenarios of Langmack data with 4, 6, 8, 12, and 18 GCPs (matrices are symmetric).

| 6 GCP | d_{kp} | d_{gcp} | d_{img} | α_{sur} | d_c | I_b | I_d |
|----------------|----------|-----------|-----------|----------------|---------|---------|---------|
| e | 0.1167 | 0.6458 | -0.1603 | 0.1643 | 0.0430 | -0.0693 | -0.1845 |
| d_{kp} | | 0.1113 | -0.2530 | 0.0499 | 0.1178 | 0.0398 | -0.0806 |
| d_{gcp} | | | -0.2447 | 0.1549 | 0.0816 | 0.0884 | -0.0150 |
| d_{img} | | | | -0.2819 | -0.1741 | -0.2108 | 0.0526 |
| α_{sur} | | | | | -0.4284 | 0.0362 | -0.4673 |
| d_c | | | | | | 0.1647 | 0.3005 |
| I_b | | | | | | | 0.4113 |

| 12 GCP | d_{kp} | d_{gcp} | d_{img} | α_{sur} | d_c | I_b | I_d |
|----------------|----------|-----------|-----------|----------------|---------|---------|---------|
| e | 0.1733 | 0.2879 | -0.3782 | 0.3057 | 0.0881 | 0.0586 | -0.2829 |
| d_{kp} | | 0.2029 | -0.2618 | 0.0502 | 0.1203 | 0.0377 | -0.0817 |
| d_{gcp} | | | -0.5186 | -0.0526 | 0.5436 | 0.1659 | 0.1405 |
| d_{img} | | | | -0.2729 | -0.1779 | -0.2085 | 0.0450 |
| α_{sur} | | | | | -0.4373 | 0.0460 | -0.4557 |
| d_c | | | | | | 0.1633 | 0.2947 |
| I_b | | | | | | | 0.4074 |

scenarios were postprocessed using SfM-MVS techniques to produce a high-resolution 3D point cloud for each scenario. Similarly, multiple SfM data sets were processed with empirical data by adjusting the number of GCPs for georeferencing and the results were studied.

The results were used to estimate the error and DPQF indexes. The error was defined as the closeness of SfM-MVS data to the ground truth model. The ground truth geometry was known precisely for the simulated scenarios, and lidar was used as the ground truth for the empirical data set. The result of the simulated data set demonstrated that the lighting condition had a distinguishable impact on 3D reconstruction error. In general, scenarios with stronger shadows or overexposed objects created more error. The reason is that both cases have featureless regions without visible texture, which locally can degrade the accuracy of the point clouds. The results of the experiments demonstrated that having the appropriate number of GCPs is essential for the accuracy of 3D reconstruction; however, overuse of GCPs may reach a point of diminishing return. The number of GCPs for dealing with an uncalibrated camera with unknown or not accurately known EO and IO seems to be essential.

To study the interrelationship of factors, the statistical relationships between the DPQFs were calculated by developing the Pearson correlation matrices for different scenarios. Some of the indexes were more influential than others. In almost all A and B simulations, there was higher correlation between error and the distance to the keypoint features and the angle of incidence factors, with correlation patterns that appeared to be similar in all simulations. The results

showed that the error is more significant in areas with a lower density of the sparse point cloud as well as on vertical surfaces with a high angle of incidence value. The empirical data had a high correlation coefficient of 0.65 between error and distance to GCP for scenarios with a smaller number of GCPs, meaning that that points with higher error were concurrent with areas were farther from GCPs. However, the error becomes independent of the number of GCPs. The remainder of error had higher correlation coefficients with the angle of incidence, darkness factor, and the number of images.

The paper introduced new quality factor indexes for assessing the accuracy of a dense point cloud by visualizing the error proxy indexes. The definition of quality factors has a tangible physical meaning that can help surveyors with planning the best data collection strategies for UAS/SfM photogrammetry. Identifying these factors during field work can help to optimize the negative factors and minimize the SfM-MVS error that may coexist with these factors.

The result of this study shows the initial development of DPQFs with the scope of indirect accuracy assessment. More studies with more comprehensive experiments are needed to draw firm conclusions about the best factors for accuracy assessment in various scenarios. Future work also could include greater spatial variations of the DPQFs for more encompassing conclusions. The advantage of the DPQFs is that the factors can be defined based solely on the inputs as results of SfM-MVS processing. The factors may provide a proxy indicator for accuracy to estimate the error for dense point

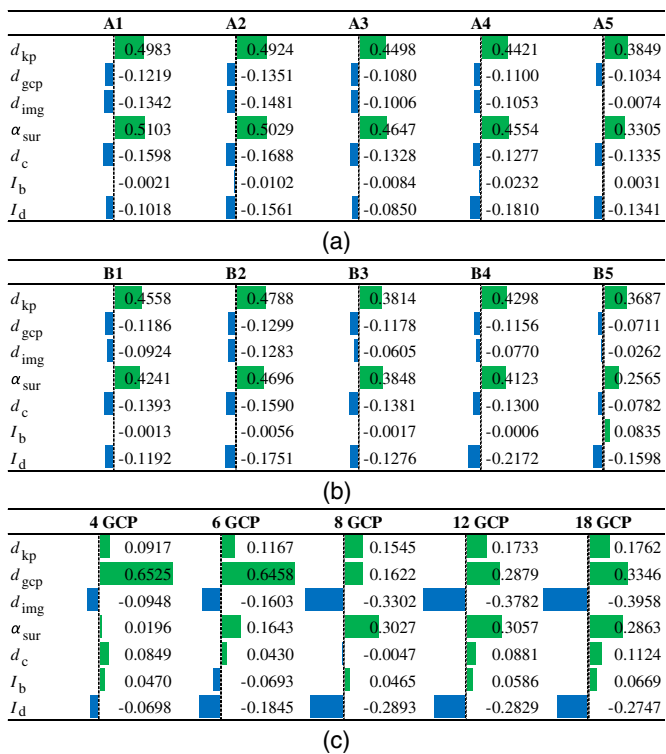


Fig. 18. Scaled bar visualization of the Pearson correlation coefficients between the 3D error and the DPQFs for (a) all simulations of A; (b) all simulations of B; and (c) scenarios of Langmack data.

clouds, which is more challenging than error propagation estimation for BA procedures due to the MVS processing.

Data Availability Statement

Some or all data, models, or code generated or used during the study are available from the corresponding author by request.

Acknowledgments

Funding for this project was provided internally by the School of Civil and Construction Engineering (CCE) at Oregon State University (OSU). The flights for the empirical case study were authorized by the FAA under license 2016-WSA-101-COA issued to OSU. The data set used for experimental data also were used for a conference publication assessing the use of UAS-based photogrammetry for generating civil integrated management (CIM) models (Javadnejad et al. 2017a). The authors thank Chase Simpson, Matthew Gillins, and Brian Weaver for their help with the field work, and Stephanie Taylor and Kevin Hamilton from Linn County Road Department, Oregon, for providing access to the site. The authors also thank Leica Geosystems, David Evans and Associates, and MicroSurvey for providing surveying equipment and/or software utilized in the experimental case study.

References

- Abellán, A., M.-H. Derron, and M. Jabolodoff. 2016. “Use of 3D point clouds in geohazards’ special issue: Current challenges and future trends.” *Remote Sens.* 8 (2): 130. <https://doi.org/10.3390/rs8020130>.
- Aguera-Vega, F., F. Carvajal-Ramírez, and P. Martínez-Carricondo. 2017. “Accuracy of digital surface models and orthophotos derived from unmanned aerial vehicle photogrammetry.” *J. Surv. Eng.* 143 (2): 04016025. [https://doi.org/10.1061/\(ASCE\)SU.1943-5428.0000206](https://doi.org/10.1061/(ASCE)SU.1943-5428.0000206).
- Anderson, M., R. Motta, S. Chandrasekar, and M. Stokes. 1996. “Proposal for a standard default color space for the internet—sRGB.” In *Proc., Color and Imaging Conf.*, 238–245. Springfield, VA: Society for Imaging Science and Technology.
- Bolkas, D. 2019. “Assessment of GCP number and separation distance for small UAS surveys with and without GNSS-PPK positioning.” *J. Surv. Eng.* 145 (3): 04019007. [https://doi.org/10.1061/\(ASCE\)SU.1943-5428.0000283](https://doi.org/10.1061/(ASCE)SU.1943-5428.0000283).
- Calì, M., and R. Ambu. 2018. “Advanced 3D photogrammetric surface reconstruction of extensive objects by UAV camera image acquisition.” *Sensors* 18 (9): 2815. <https://doi.org/10.3390/s18092815>.
- Carboneau, P. E., and J. T. Dietrich. 2017. “Cost-effective non-metric photogrammetry from consumer-grade sUAS: Implications for direct georeferencing of structure from motion photogrammetry.” *Earth Surf. Processes Landforms* 42 (3): 473–486. <https://doi.org/10.1002/espl.4012>.
- Che, E., and M. J. Olsen. 2017. “Fast ground filtering for TLS data via scanline density analysis.” *ISPRS J. Photogramm. Remote Sens.* 129 (Jul): 226–240. <https://doi.org/10.1016/j.isprsjprs.2017.05.006>.
- Chudley, T. R., P. Christoffersen, S. H. Doyle, A. Abellan, and N. Snooke. 2019. “High-accuracy UAV photogrammetry of ice sheet dynamics with no ground control.” *Cryosphere* 13 (3): 955–968. <https://doi.org/10.5194/tc-13-955-2019>.
- Clapuyt, F., V. Vanacker, and K. Van Oost. 2016. “Reproducibility of UAV-based earth topography reconstructions based on Structure-from-Motion algorithms.” *Geomorphology* 260 (May): 4–15. <https://doi.org/10.1016/j.geomorph.2015.05.011>.
- Colomina, I., and P. Molina. 2014. “Unmanned aerial systems for photogrammetry and remote sensing: A review.” *ISPRS J. Photogramm. Remote Sens.* 92 (Jun): 79–97. <https://doi.org/10.1016/j.isprsjprs.2014.02.013>.
- Crandall, D. J., A. Owens, N. Snavely, and D. P. Huttenlocher. 2013. “SfM with MRFs: Discrete-continuous optimization for large-scale structure from motion.” *IEEE Trans. Pattern Anal. Mach. Intell.* 35 (12): 2841–2853. <https://doi.org/10.1109/TPAMI.2012.218>.
- Dandois, J., M. Olano, and E. Ellis. 2015. “Optimal altitude, overlap, and weather conditions for computer vision UAV estimates of forest structure.” *Remote Sens.* 7 (10): 13895–13920. <https://doi.org/10.3390/rs71013895>.
- Eltner, A., A. Kaiser, C. Castillo, G. Rock, F. Neugirg, and A. Abellán. 2016. “Image-based surface reconstruction in geomorphometry—Merits, limits and developments.” *Earth Surf. Dyn.* 4 (2): 359–389. <https://doi.org/10.5194/esurf-4-359-2016>.
- Faraji, M. R., X. Qi, and A. Jensen. 2016. “Computer vision-based orthorectification and georeferencing of aerial image sets.” *J. Appl. Remote Sens.* 10 (3): 036027. <https://doi.org/10.1117/1.JRS.10.036027>.
- Fischler, M. A., and R. C. Bolles. 1981. “Random sample consensus: A paradigm for model fitting with applications to image analysis and automated cartography.” *Commun. ACM* 24 (6): 381–395. <https://doi.org/10.1145/358669.358692>.
- Fonstad, M. A., J. T. Dietrich, B. C. Courville, J. L. Jensen, and P. E. Carboneau. 2013. “Topographic structure from motion: A new development in photogrammetric measurement.” *Earth Surf. Processes Landforms* 38 (4): 421–430. <https://doi.org/10.1002/esp.3366>.
- Furukawa, Y., and J. Ponce. 2010. “Accurate, dense, and robust multiview stereopsis.” *IEEE Trans. Pattern Anal. Mach. Intell.* 32 (8): 1362–1376. <https://doi.org/10.1109/TPAMI.2009.161>.
- Gao, M., X. Xu, Y. Klinger, J. van der Woerd, and P. Tapponnier. 2017. “High-resolution mapping based on an unmanned aerial vehicle (UAV) to capture paleoseismic offsets along the Altyn-Tagh fault, China.” *Sci. Rep.* 7 (1): 8281. <https://doi.org/10.1038/s41598-017-08119-2>.
- González-Quiñones, J., J. Reinoso-Gordo, C. León-Robles, J. García-Balboa, and F. Ariza-López. 2018. “Variables influencing the accuracy of 3D modeling of existing roads using consumer cameras in aerial photogrammetry.” *Sensors* 18 (11): 3880. <https://doi.org/10.3390/s18113880>.

- Griffin, G. F. 2014. "The use of unmanned aerial vehicles for disaster management." *Geomatica* 68 (4): 265–281. <https://doi.org/10.5623/cig2014-402>.
- Harris, C., and M. Stephens. 1988. "A combined corner and edge detector." In Vol. 15 of *Proc., Alvey Vision Conf.* Oxen, UK: Alvey Vision Club.
- Harwin, S., and A. Lucieer. 2012. "Assessing the accuracy of georeferenced point clouds produced via multi-view stereopsis from unmanned aerial vehicle (UAV) imagery." *Remote Sens.* 4 (6): 1573–1599. <https://doi.org/10.3390/rs4061573>.
- Harwin, S., A. Lucieer, and J. Osborn. 2015. "The impact of the calibration method on the accuracy of point clouds derived using unmanned aerial vehicle multi-view stereopsis." *Remote Sens.* 7 (9): 11933–11953. <https://doi.org/10.3390/rs70911933>.
- Hofsetz, C., K. Ng, G. Chen, P. McGuinness, N. Max, and Y. Liu. 2004. "Image-based rendering of range data with estimated depth uncertainty." *IEEE Comput. Graphics Appl.* 24 (4): 34–41. <https://doi.org/10.1109/MCG.2004.8>.
- James, M. R., S. Robson, S. D'Oleire-Oltmanns, and U. Niethammer. 2017a. "Optimising UAV topographic surveys processed with structure-from-motion: Ground control quality, quantity and bundle adjustment." *Geomorphology* 280 (Mar): 51–66. <https://doi.org/10.1016/j.geomorph.2016.11.021>.
- James, M. R., S. Robson, and M. W. Smith. 2017b. "3-D uncertainty-based topographic change detection with structure-from-motion photogrammetry: Precision maps for ground control and directly georeferenced surveys." *Earth Surf. Processes Landforms* 42 (12): 1769–1788. <https://doi.org/10.1002/esp.4125>.
- Javadnejad, F. 2018. "Small unmanned aircraft systems (UAS) for engineering inspections and geospatial mapping." Ph.D. dissertation, School of Civil and Construction Engineering, Oregon State Univ.
- Javadnejad, F., and D. T. Gillins. 2016. "Unmanned aircraft systems-based photogrammetry for ground movement monitoring." In *Proc., Pipelines 2016*, 1000–1011. Reston, VA: ASCE.
- Javadnejad, F., D. T. Gillins, C. E. Parrish, and R. K. Slocum. 2019. "A photogrammetric approach to fusing natural colour and thermal infrared UAS imagery in 3D point cloud generation." *Int. J. Remote Sens.* 41 (1): 211–237. <https://doi.org/10.1080/01431161.2019.1641241>.
- Javadnejad, F., M. N. Gillins, and D. T. Gillins. 2016. "Vertical accuracy assessment of image-based reconstructed 3D point clouds with respect to horizontal ground sampling distance." In *Proc., ASPRS Annual Conf., Imaging & Geospatial Technology Forum (IGTF) 2016*. Fort Worth, TX: American Society for Photogrammetry and Remote Sensing.
- Javadnejad, F., C. H. Simpson, D. T. Gillins, T. Claxton, and M. J. Olsen. 2017a. "An assessment of UAS-based photogrammetry for civil integrated management (CIM) modeling of pipes." In *Proc., Pipelines 2017*, 112–123. Reston, VA: ASCE.
- Javadnejad, F., B. Waldron, and A. Hill. 2017b. "LITE flood: Simple GIS-based mapping approach for real-time redelineation of multifrequency floods." *Nat. Hazards Rev.* 18 (3): 04017004. [https://doi.org/10.1061/\(ASCE\)NH.1527-6996.0000238](https://doi.org/10.1061/(ASCE)NH.1527-6996.0000238).
- Javadnejad, F., B. A. Waldron, and F. Alinia. 2013. "GIS-based gold potential mapping in the Muteh Deposit Area, Iran, with respect to a new mineralization concept." In *Proc., 2013 4th Int. Conf. on Computing for Geospatial Research and Application*, 148–149. New York: IEEE.
- Lague, D., N. Brodu, and J. Leroux. 2013. "Accurate 3D comparison of complex topography with terrestrial laser scanner: Application to the Rangitikei canyon (N-Z)." *ISPRS J. Photogramm. Remote Sens.* 82 (Aug): 10–26. <https://doi.org/10.1016/j.isprsjprs.2013.04.009>.
- LINZ (Land Information New Zealand). 2016. "Invercargill 0.1m urban aerial photos (2016)." Accessed January 1, 2017. <https://data.linz.govt.nz/layer/88147-invercargill-01m-urban-aerial-photos-2016/>.
- Lowe, D. G. 1999. "Object recognition from local scale-invariant features." In *Proc., 7th IEEE Int. Conf. on Computer Vision*, 1150–1157. New York: IEEE.
- Lowe, D. G. 2004. "Distinctive image features from scale-invariant keypoints." *Int. J. Comput. Vision* 60 (2): 91–110. <https://doi.org/10.1023/B:VISI.0000029664.99615.94>.
- Mahmoudabadi, H., M. J. Olsen, and S. Todorovic. 2016. "Efficient terrestrial laser scan segmentation exploiting data structure." *ISPRS J. Photogramm. Remote Sens.* 119 (Sep): 135–150. <https://doi.org/10.1016/j.isprsjprs.2016.05.015>.
- McCaffrey, K. J. W., R. R. Jones, R. E. Holdsworth, R. W. Wilson, P. Clegg, J. Imber, N. Holliman, and I. Trinks. 2005. "Unlocking the spatial dimension: Digital technologies and the future of geoscience fieldwork." *J. Geol. Soc.* 162 (6): 927–938. <https://doi.org/10.1144/0016-764905-017>.
- O'Banion, M. S., M. J. Olsen, C. E. Parrish, and M. Bailey. 2019. "Interactive visualization of 3D coordinate uncertainties in terrestrial laser scanning point clouds using OpenGL shader language." *J. Surv. Eng.* 145 (1): 04018012. [https://doi.org/10.1061/\(ASCE\)SU.1943-5428.0000267](https://doi.org/10.1061/(ASCE)SU.1943-5428.0000267).
- O'Banion, M. S., M. J. Olsen, C. Rault, J. Wartman, and K. Cunningham. 2018. "Suitability of structure from motion for rock-slope assessment." *Photogramm. Rec.* 33 (162): 217–242. <https://doi.org/10.1111/phor.12241>.
- Olsen, M., J. Wartman, M. McAlister, H. Mahmoudabadi, M. O'Banion, L. Dunham, and K. Cunningham. 2015. "To fill or not to fill: Sensitivity analysis of the influence of resolution and hole filling on point cloud surface modeling and individual rockfall event detection." *Remote Sens.* 7 (9): 12103–12134. <https://doi.org/10.3390/rs70912103>.
- Omata, K., F. Hosoi, and A. Konishi. 2006. "3D lidar imaging for detecting and understanding plant responses and canopy structure." *J. Exp. Bot.* 58 (4): 881–898. <https://doi.org/10.1093/jxb/erl142>.
- Oregon Department of Transportation (ODOT). 2020. "Oregon real-time GNSS network (ORGN)." Accessed September 2, 2020. <https://www.oregon.gov/odot/orgn/pages/index.aspx>.
- OuYang, D., and H.-Y. Feng. 2005. "On the normal vector estimation for point cloud data from smooth surfaces." *Comput.-Aided Des.* 37 (10): 1071–1079. <https://doi.org/10.1016/j.cad.2004.11.005>.
- Pajares, G. 2015. "Overview and current status of remote sensing applications based on unmanned aerial vehicles (UAVs)." *Photogramm. Eng. Remote Sens.* 81 (4): 281–330. <https://doi.org/10.14358/PERS.81.4.281>.
- Rangel, J. M. G., G. R. Gonçalves, and J. A. Pérez. 2018. "The impact of number and spatial distribution of GCPs on the positional accuracy of geospatial products derived from low-cost UASs." *Int. J. Remote Sens.* 39 (21): 7154–7171. <https://doi.org/10.1080/01431161.2018.1515508>.
- Remondino, F., M. G. Spera, E. Nocerino, F. Menna, and F. Nex. 2014. "State of the art in high density image matching." *Photogramm. Rec.* 29 (146): 144–166. <https://doi.org/10.1111/phor.12063>.
- Sanz-Ablanedo, E., J. Chandler, J. Rodríguez-Pérez, and C. Ordóñez. 2018. "Accuracy of unmanned aerial vehicle (UAV) and SfM photogrammetry survey as a function of the number and location of ground control points used." *Remote Sens.* 10 (10): 1606. <https://doi.org/10.3390/rs10101606>.
- Seitz, S. M., B. Curless, J. Diebel, D. Scharstein, and R. Szeliski. 2006. "A comparison and evaluation of multi-view stereo reconstruction algorithms." In Vol. 1 of *Proc., 2006 IEEE Computer Society Conf. on Computer Vision and Pattern Recognition (CVPR'06)*, 519–528. New York: IEEE.
- Shi, Y., et al. 2016. "Unmanned aerial vehicles for high-throughput phenotyping and agronomic research." *PLoS One* 11 (7): e0159781. <https://doi.org/10.1371/journal.pone.0159781>.
- Shum, H.-Y., Q. Ke, and Z. Zhang. 1999. "Efficient bundle adjustment with virtual key frames: A hierarchical approach to multi-frame structure from motion." In *Proc., 1999 IEEE Computer Society Conf. on Computer Vision and Pattern Recognition (Cat. No PR00149)*, 538–543. New York: IEEE.
- Slocum, R. K., and C. E. Parrish. 2017. "Simulated imagery rendering workflow for UAS-based photogrammetric 3D reconstruction accuracy assessments." *Remote Sens.* 9 (4): 396. <https://doi.org/10.3390/rs9040396>.
- Smith, M. W., and D. Vericat. 2015. "From experimental plots to experimental landscapes: Topography, erosion and deposition in sub-humid badlands from structure-from-motion photogrammetry." *Earth Surf. Processes Landforms* 40 (12): 1656–1671. <https://doi.org/10.1002/esp.3747>.
- Snavely, N., S. M. Seitz, and R. Szeliski. 2006. "Photo tourism." In *Proc., ACM SIGGRAPH 2006 Papers on—SIGGRAPH '06*, 835. New York: ACM Press.
- Snavely, N., S. M. Seitz, and R. Szeliski. 2008. "Modeling the world from internet photo collections." *Int. J. Comput. Vision* 80 (2): 189–210. <https://doi.org/10.1007/s11263-007-0107-3>.

- Sohn, G., and I. Dowman. 2007. "Data fusion of high-resolution satellite imagery and LiDAR data for automatic building extraction." *ISPRS J. Photogramm. Remote Sens.* 62 (1): 43–63. <https://doi.org/10.1016/j.isprsjprs.2007.01.001>.
- Szeliski, R. 2010. *Computer vision: Algorithms and applications*. New York: Springer.
- Tomasi, C., and T. Kanade. 1992. "Shape and motion from image streams under orthography: A factorization method." *Int. J. Comput. Vision* 9 (2): 137–154. <https://doi.org/10.1007/BF00129684>.
- Tonkin, T., and N. Midgley. 2016. "Ground-control networks for image based surface reconstruction: An investigation of optimum survey designs using UAV derived imagery and structure-from-motion photogrammetry." *Remote Sens.* 8 (9): 786. <https://doi.org/10.3390/rs8090786>.
- Triggs, B., P. F. McLauchlan, R. I. Hartley, and A. W. Fitzgibbon. 1999. "Bundle adjustment—A modern synthesis." In *Proc., Int. Workshop on Vision Algorithms*, 298–372. Berlin: Springer.
- Westoby, M. J., J. Brasington, N. F. Glasser, M. J. Hambrey, and J. M. Reynolds. 2012. "'Structure-from-Motion' photogrammetry: A low-cost, effective tool for geoscience applications." *Geomorphology* 179 (Dec): 300–314. <https://doi.org/10.1016/j.geomorph.2012.08.021>.
- Wood, R. L., D. T. Gillins, M. E. Mohammadi, F. Javadnejad, H. Tahami, M. N. Gillins, and Y. Liao. 2017. "2015 Gorkha post-earthquake reconnaissance of a historic village with micro unmanned aerial systems." In *Proc., 16th World Conf. on Earthquake (16WCEE)*. Tokyo: International Association for Earthquake Engineering.
- Yao, Y., H. Zhu, Y. Nie, X. Ji, and X. Cao. 2014. "Revised depth map estimation for multi-view stereo." In *Proc., 2014 Int. Conf. on 3D Imaging (IC3D)*, 1–7. New York: IEEE.
- Zhu, Z., C. Stamatopoulos, and C. S. Fraser. 2015. "Accurate and occlusion-robust multi-view stereo." *ISPRS J. Photogramm. Remote Sens.* 109 (Nov): 47–61. <https://doi.org/10.1016/j.isprsjprs.2015.08.008>.